TRIBHUVAN UNIVERSITY
INSTITUTE OF ENGINEERING
PULCHOWK CAMPUS

Design and Experiment of Negative-Stiffness Electromagnetic Spring for Low-Frequency Vibration Isolation

By:
Aayush Subedi (077BME002)
Rachit Rijal (077BME027)
Ravin Kumar Purbey (077BME030)
Tulsi Narayan Shrestha (077BME045)

A PROJECT REPORT
SUBMITTED TO THE DEPARTMENT OF MECHANICAL AND AEROSPACE ENGINEERING IN PARTIAL FULFILLMENT OF THE REQUIREMENT FOR THE DEGREE OF BACHELOR IN MECHANICAL ENGINEERING

DEPARTMENT OF MECHANICAL AND AEROSPACE ENGINEERING
LALITPUR, NEPAL

April 2025

COPYRIGHT

The author has agreed that the library, Department of Mechanical and Aerospace Engineering, Pulchowk Campus, Institute of Engineering, may make this project report freely available for inspection. Moreover, the author has agreed that permission for extensive copying of this project report for scholarly purpose may be granted by the professor(s) who supervised the work recorded herein or, in their absence, by the Head of the Department wherein the thesis was done. It is understood that the recognition will be given to the author of this project report and the Department of Mechanical and Aerospace Engineering, Pulchowk Campus, Institute of Engineering, in any use of the material of this project report. Copying, publishing, or using this project report for financial gain without approval of the Department of Mechanical and Aerospace Engineering, Pulchowk Campus, Institute of Engineering, and the author's written permission is prohibited. Request for permission to copy or to make any other use of this project report, in whole or in part, should be addressed to: Head of Department Department of Mechanical and Aerospace Engineering Pulchowk Campus, Institute of Engineering Lalitpur, Kathmandu Nepal

LETTER OF APPROVAL

TRIBHUVAN UNIVERSITY
INSTITUTE OF ENGINEERING
CENTRAL CAMPUS PULCHOWK
DEPARTMENT OF MECHANICAL AND AEROSPACE ENGINEERING

The undersigned certify that they have read, and recommended to the Institute of Engineering for acceptance, a project report entitled **"Design and Experiment of Negative-Stiffness Electromagnetic Spring for Low-Frequency Vibration Isolation"** submitted by Aayush Subedi, Rachit Rijal, Ravin Kumar Purbey and Tulsi Narayan Shrestha in partial fulfillment of the requirements for the degree of Bachelor of Mechanical Engineering.

Supervisor, Dr. Mahesh Chandra Luintel
Professor
Department of Mechanical and Aerospace Engineering
Institute of Engineering, Pulchowk Campus

External Examiner, Shailendra Shah
Mechanical Engineer
National Vigilance Centre

Head of Department, Dr. Sudip Bhattrai
Assistant Professor
Department of Mechanical and Aerospace Engineering
Institute of Engineering, Pulchowk Campus

Date: March 11, 2025

ACKNOWLEDGEMENT

We would like to express our sincere gratitude to the Department of Mechanical and Aerospace Engineering at IOE, Pulchowk Campus, for providing us with the opportunity to undertake a project that bridges theoretical knowledge with practical applications, further enhancing our understanding of advanced engineering concepts.

Our deepest appreciation goes to Professor Dr. Mahesh Chandra Luitel, Lecturer Biman Rimal, Mr. Aayush Bhatta, Mr. Chandrika Nand Adhikari, Mr. Ghanshyam Aryal, and Mr. Salim Maharjan for their invaluable guidance and insightful feedback on our project. Their expert advice has played a pivotal role in shaping its direction.

We extend our sincere gratitude to Litmus Cables for their in-kind sponsorship of enameled copper winding wire, which was essential to the completion of this project and will support similar future research within the department. We also thank Er. Dipesh Nepal in particular for his continued patience, support, and enthusiasm.

We also gratefully acknowledge Mr. Suraj Neuapne for his invaluable assistance in the procurement of mechanical springs, which will support future vibration experiments in the Dynamics Lab.

We also wish to extend our heartfelt thanks to our friends Able Khanal, Anunaya Gartaula, Himal Timsina, Manish Tajpuria, Someet Sharma Thakur, Nripesh Dhungana, and Prashant Sharma for their continuous support and constructive recommendations, which have significantly contributed to various aspects of our work.

Additionally, we are grateful to the faculty members of the Dynamics Lab for their readiness to assist and for providing us with access to the necessary equipment and facilities, which are essential for the successful completion of our project.

ABSTRACT

This study presents the design, modeling, and experimental validation of a tunable negative-stiffness based vibration isolator using a multi-layer Electromagnetic Spring Assembly (ESA). Mathematical models based on the filament method were implemented in Python to predict axial force-displacement and (negative) stiffness-displacement relationships for various ESA configurations. Validation of the analytical model against Ansys Maxwell simulations and load-cell measurements demonstrated average errors of 16.4% and 5.33% respectively. Dynamic modeling and curve fitting closely approximated the force as a cubic equation with a high degree of accuracy ($R^2 > 0.99998$). The negative stiffness region for various ESA configurations broadened by increasing the number of layers in the assembly or increasing the current through the coils. For a 6-layer Unipolar ESA (UESA), peak negative stiffness of $-109.307\ N/m$ was recorded while that for a 6-layer Alternating Polarity (AESA) reached $-469.9\ N/m$ at $4A$ control current.

A modular working prototype of the vibration isolator was fabricated using N35 permanent ring magnets, copper coils(SWG 16), and a mechanical spring ($k = 2.277\ kN/m$), and a 3D-printed PLA body along with a spring-supported plywood shake table. Under sinusoidal excitation, baseline payload acceleration of 4.50 m/s^2 at 10 Hz reduced to 2.00 m/s^2 ($3A$) , 1.73 m/s^2 ($3.5A$), and 1.48 m/s^2 ($4A$), corresponding to up to 67% attenuation, demonstrating current-based tunable vibration isolation capabilities.

The prototype presents the case for the use of ESA to significantly reduce low-frequency vibrations and offers a modular and tunable solution for industrial and academic applications.

Keywords: *Vibration Isolation, Negative Stiffness, Electromagnet, Filament Method*

TABLE OF CONTENTS

LIST OF TABLES

LIST OF FIGURES

LIST OF ABBREVIATIONS

AESA	Alternate Electromagnetic Spring Assembly
B K	Bruel & Kjær
DAQ	Data Acquisition
DC	Direct Current
ER	Electrorheologica
ESA	Electromagnetic Spring Assembly
FEA	Finite Element Analysis
HSLDS	High Static Low Dynamic Stiffness
LES	Linear Electromagnetic Spring
MES	Multi-layer Electromagnetic Spring
MR	Magnetorheologica
MSNS	Magnetic Spring with Negative Stiffness
NS	Negative Stiffness
NSVID	Negative Stiffness Vibration Isolation Device
QZS	Quasi-Zero Static
RMSE	Root Mean Square Error
UESA	Uniform Electromagnetic Spring Assembly
UNF	Unified National Fine

CHAPTER 1

INTRODUCTION

1.1 Background

1.1.1 Vibration Isolation

Unwanted vibrations are a persistent problem in engineering, as they can degrade the performance, precision, and durability of mechanical systems. Sensitive instruments lose accuracy, noise levels increase, and wear accelerates due to these disturbances. Vibration isolation is essential for reducing the transmission of vibrations to protected systems. Traditionally, this has been achieved by lowering the system's natural frequency below the excitation frequency using a combination of springs and dampers.

While passive vibration isolation systems are simple and cost-effective, they struggle with low-frequency vibrations. Active vibration isolators use sensors and actuators to counter vibrations in real-time, offering high performance but at increased energy consumption and cost. Semi-active systems provide a balanced solution by dynamically adjusting stiffness and damping, making them effective for applications such as precision manufacturing, automotive systems, and laboratory equipment.

Negative Stiffness Device for Vibration Isolation:

Negative stiffness mechanisms (NSMs) have recently received considerable attention in solving a problem that traditional systems face: low- and ultra-low-frequency vibrations. Some of the ways in which negative stiffness can be realized include using mechanical systems, magnetic structures, or composite materials. These mechanisms, when combined with a positive stiffness mechanism constitute a system with High-Static-Low-Dynamic-Stiffness (HSLDS) characteristic.

HSLDS systems comprise a quasi-zero stiffness (QZS) region in the force-displacement curve and provide excellent vibration isolation at low frequency. They also improve damping and energy absorption, and find applications in precision instruments, aerospace, and laboratory setups. Innovations in NSMs, especially those using magnetic and electromagnetic elements, have led to more compact, modular, and tunable vibration isolation designs.

1.1.2 Electromagnetic Spring Assembly (ESA)

By using coaxially arranged permanent magnets and electromagnetic coils, an Electromagnetic Spring Assembly(ESA) generates negative stiffness that can be adjusted by controlling the current through the coils. This ability to adjust the stiffness allows the ESA to adapt to different vibration profiles with high efficiency and precision.

A key feature of an ESA is its contactless operation, which eliminates mechanical wear and ensures long-term durability. Additionally, an ESA can be adapted in a modular design, incorporating various numbers and configurations of current-carrying coils and permanent magnets. This assembly offers significant flexibility, making it possible to customize the system to meet specific performance requirements.

1.2 Problem Statement

Industries such as manufacturing, aerospace, and instrumentation require precise, tunable vibration isolation systems for low-frequency vibrations ($\leq 20\ \text{Hz}$). An electromagnetic spring enables adjustable negative stiffness and, as an extension, customizable vibration isolation properties. With its contactless operation, minimized mechanical wear, and enhanced durability, an Electromagnetic Spring Assembly (ESA)-based isolator is well-suited for both academic research and real-world industrial applications. Additionally, a vibration isolator incorporating such an assembly is designed to be highly modular in both strength and configuration.

This project focuses on designing and fabricating an Electromagnetic Spring Assembly-based vibration isolator for the Dynamics Lab at the Department of Mechanical and Aerospace Engineering. The system will provide students and researchers with a hands-on platform to study and experiment with vibration control systems.

1.3 Objectives

1.3.1 Main Objective

To design, fabricate, and test a negative-stiffness electromagnetic spring for low-frequency vibration isolation.

1.3.2 Specific Objectives

- To design a negative-stiffness electromagnetic spring and determine its force and stiffness characteristics.
- To derive the mathematical relationship for the stiffness of the electromagnetic system as a function of the displacement of permanent magnet(s) from an equi-

librium position.

- To design and fabricate a vibration isolator prototype incorporating the electromagnetic spring as well as a mechanical spring
- To measure acceleration values before and after isolator activation to evaluate its effectiveness in reducing low-frequency vibrations.

1.4 System Requirements

Hardware Requirements

- Mechanical Components
    - Mechanical spring of various stiffness rates (ranging from 2 kN/m to 10 kN/m),
    - Stainless steel shaft (8 mm),
    - Linear bushing (15 mm),
    - Linear bearing (8 mm),
    - Nylon collars (8 mm),
    - PLA filaments,
    - Shake table.
- Electronic/Magnetic Components
    - Accelerometer: B&K Type 4371 ,
    - Charge amplifier: B&K Type 2635,
    - NI myDAQ Student Data Acquisition Device,
    - Neodymium magnets: N35 permanent ring magnets (inner diameter: 10 mm, outer diameter: 28 mm, height: 10.5 mm),
    - Copper coil: Enameled Copper Winding, SWG 16,
    - Programmable DC Power Supply: SIGLENT SPD1305X,
    - Waveform Generator SIGLENT SDG6022X
    - Vibration Exciter B&K Type 4809
    - Multimeter.

Software Requirements

- ANSYS Mechanical, Maxwell 2024R2
- Solidworks 2024
- Arduino IDE

- MATLAB R2021a
- Google Colab
- Visual Studio Code 17.12.2
- NI LabView 2022 Q3
- NI DAQmx 2022 Q3
- Python 3, with the following modules:
  - NumPy
  - Pandas
  - SciPy
  - Matplotlib

CHAPTER 2

LITERATURE REVIEW

2.1 Vibration Isolation

Vibration isolation plays a key role in mechanical engineering by minimizing the transmission of vibrations from their source to a receiver. This is essential in industries where reducing vibrations improves equipment reliability, increases user comfort, and extends machinery lifespan.

Based on how the vibration isolator manages and controls vibrations, it is classified into the following:

Active Isolation: Active vibration isolators use actuators to apply controlled forces to cancel out transmitted vibrations, making them highly adaptable to various conditions. However, they come with trade-offs, such as high power consumption and the risk of instability under certain circumstances. Despite these challenges, active vibration isolation systems are widely used in applications like spacecraft, tall buildings to prevent excessive swaying, and car suspension systems to improve stability and comfort.

Semi-active Isolation: Semi-active isolators combine the robustness of passive systems with the versatility of active systems, and require minimal external power to adjust stiffness or damping coefficients. This adjustment is often achieved using Electrorheological (ER) and Magnetorheological (MR) fluids, which change viscosity when subjected to electrical or magnetic fields, respectively [4], [5].

Passive Isolation: Passive vibration isolators are commonly preferred in engineering applications because they are simple, do not require external power or computer control, and are cost-effective. These systems typically rely on load-supporting elements and energy-dissipating components, often integrating both functions into mounts made of rubber. Rubber mounts are durable and space-efficient but present complexities due to their visco-elastic behavior. Other options, like helical springs and air springs, also have unique advantages and disadvantages.

2.2 HSLDS Mechanism

In an ideal scenario where a mass m is supported by a linear stiffness k on a firm foundation, isolation isn't achieved until a frequency of $\sqrt{2}\omega_n$ is reached, where ω_n is the undamped natural frequency of the isolator. It is apparent that decreasing stiffness widens the range of isolation frequencies. However, reducing stiffness also increases the static displacement of the mass.

A desirable vibration isolator should possess high-static–low-dynamic stiffness (HSLDS) so that it can support a large load statically while having low dynamic stiffness. An HSLDS spring is essentially a non-linear spring that varies its stiffness non-linearly (say, quadratically) with displacement, allowing for the same static displacement as a linear spring but exhibiting lower dynamic stiffness for small oscillations around the static equilibrium.

When an isolator has zero or near-zero dynamic stiffness, it is referred to as a quasi-zero-stiffness (QZS) isolator. There are a number of ways to obtain the HSLDS property. A common method to design a passive HSLDS isolator is to combine a positive stiffness spring with a negative stiffness spring.

2.3 Negative Stiffness Mechanism

Negative stiffness is essential for Quasi-Zero-Stiffness (QZS) vibration isolators. While the negative stiffness mechanism lacks load-bearing capacity and undergoes significant deformation under any load, it can be combined with a positive stiffness mechanism to counteract instability.

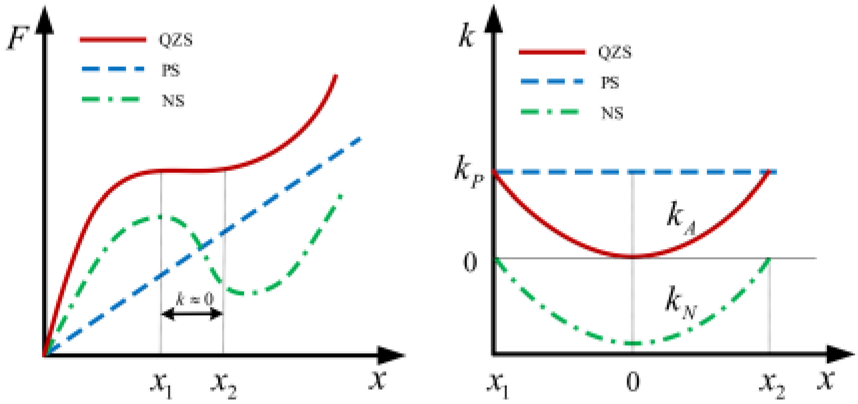

Figure 2.1: Principle of QZS vibration isolator: Force-displacement relationship *(left)*; Stiffness Displacement relationship *(right)* [1].

Different many methods of achieving negative stiffness are discussed in the following sections.

2.3.1 Mechanical Spring

In order to counteract the positive stiffness that the vertical spring provided, Carrela et al. [6] used two oblique springs to create negative stiffness. The isolator's force and displacement transmissibility were also examined in a later work [7].

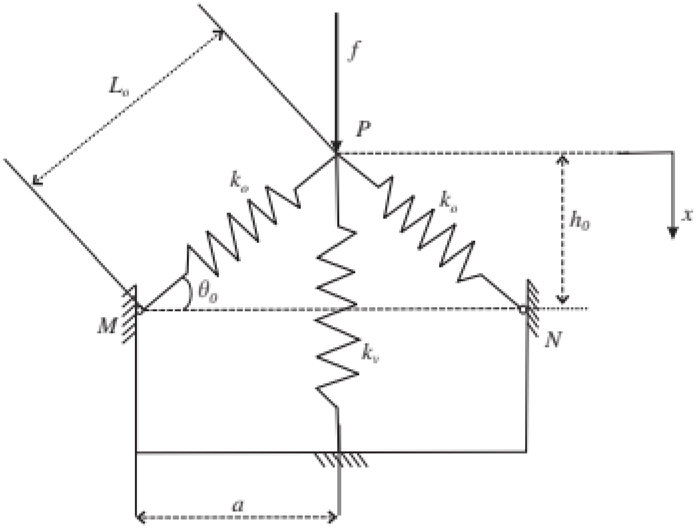

Figure 2.2: Schematic for analytical treatments of spring-based QZS isolators [2]

Although difficulties in quantifying damping were observed, a hinged horizontal beam with adjustable negative rotational stiffness achieved very low-frequency oscillation in [6], greatly lowering the oscillation frequency of the system. Nonlinear pre-stressed oblique springs were used in [7] to improve quasi-zero-stiffness (QZS) mechanisms. This resulted in near-zero stiffness near equilibrium and smaller stiffness at larger displacements (optimal inclination angles of 48°–57°), which improved both static and dynamic isolation performance.

Approximate analytical methods for a system, a simple system consisting of a vertical spring acting in parallel with two oblique springs, were explored by Carrela et al. [2] and Kovacic et al. [8], respectively. Kovacic et al. [8] demonstrated that a cubic equation can be used to approximate the system's force–displacement characteristic.

2.3.2 Pre-Buckled Beam

Huang et al. [9] investigated a quasi-zero stiffness isolator using Euler buckled beams as negative stiffness correctors theoretically and experimentally.

2.3.3 Bio-Inspired Structure

Dai et al. [10] designed a bionic vibration isolator, inspired by the symmetrical, limb-like structure of kangaroo legs. They systematically explored its beneficial nonlinear stiffness for low-frequency or ultra-low-frequency vibration isolation. Sun and Ge et al. [11] proposed a polygonal skeleton structure inspired by the biological structure of the legs of bipeds.

2.3.4 Composite Structure

Currently, various types of quasi-zero stiffness (QZS) vibration isolators utilizing composite structures have been developed, primarily comprising honeycomb and unit cell configurations [12], [13].

2.3.5 Magnetic Structure

HSLDS vibration isolators incorporating magnetic and electromagnetic structures are of particular interest and will be discussed briefly in the following sections.

By using three permanent magnets that were in attractive interaction in the vertical direction, Carrella et al. [14] combined mechanical springs and magnets to reduce the sysetm's natural frequency from 14 Hz to 7 Hz, maintaining linear transmissibility. Zhou and Liu [15] proposed a negative stiffness magnetic spring (NSMS) composed of two electromagnets and a permanent magnet, which was mounted in parallel with a structural beam as the mechanical spring. Said isolator was capable of both off-line and on-line tuning by adjusting the gap distance and current, respectively. Zheng et al. [16] employed a pair of coaxial tile magnets of equal height, installed in parallel with a mechanical spring, to reduce the resonance frequency from 9.0 Hz to 5.8 Hz.

2.3.6 Electromagnetic Structure

Zhou and Liu [15] proposed a negative stiffness magnetic spring (NSMS). Their design used two electromagnets and one permanent magnet mounted parallel to a beam. The isolator is tuned offline by adjusting the gap distance and online by changing the current.

Yuan et al. [17] developed a quasi-zero-stiffness (QZS) vibration isolator by integrating a linear electromagnetic spring with a traditional isolator. The spring consisted of three toroidal coils and a ring magnet. By varying the coil current, they tuned the natural frequency from 2 Hz to 10 Hz, which improved vibration isolation.

Similarly, Sun et al. [18] used coaxial coil windings and ring-shaped permanent magnets to achieve negative stiffness. They demonstrated that increasing the coil current further reduces vibrations.

Pu et al. [19] designed a multi-layer electromagnetic spring (MES) with tunable stiffness. The 6-layer MES achieved a stiffness of ±9800 N/m at ±1.2 A, with a natural frequency tunable from 8.8 Hz to 2.6 Hz and provided a 3.8 Hz isolation band.

Across these studies, electromagnetic springs were modeled using analytical methods such as the filament method or Ampère's current model. These models were validated by experiments. Performance of the vibration isolator was then evaluated by measuring transmissibility and natural frequency.

2.4 Electromagnetic Spring Assembly (ESA)

A single unit or layer of an electromagnetic spring assembly consists of a coaxially arranged permanent magnet ring and an electric coil. The permanent magnet is axially magnetized, while the coil is the solenoid, with a controllable current passing through it. Such a single unit is often referred to as a **Linear Electromagnetic Spring (LES)** because it generally operates within a range where the behavior of the system is linear.

The electromagnetic force in the ESA is governed by the current supplied to the coil. The system achieves an equilibrium position when the relative displacement (D) between the magnet and the coil is zero. If a small disturbance occurs, the electromagnetic force repels the magnet, causing it to move away from this equilibrium.

The negative stiffness characteristic of an ESA unit is achieved by controlling the coil current or modifying the configuration of ESA units - for example, by stacking multiple units or altering the effective magnetic polarity of each unit. The design is such that the direction of the electromagnetic force is opposite to the relative displacement of the magnet, representing a negative stiffness behavior. In this mechanism, the applied electromagnetic force decreases as the magnet moves further away from equilibrium, which contrasts with positive stiffness systems, where the force increases with displacement.

The negative stiffness in the ESA is directly proportional to the current supplied to the coil, as shown in subsequent analyses. By combining an ESA in parallel with a mechanical spring that provides positive stiffness, the resulting system exhibits an overall stiffness lower than the mechanical spring alone. This combined configuration is key for vibration isolation applications. Interestingly, reversing the current polarity in the coil allows the ESA to exhibit positive stiffness behavior when needed.

The design of a vibration isolator using ESA units is centered on their negative stiffness characteristics. Analytical models are used to calculate these characteristics, which are then validated through simulations and experiments. This forms the basis for designing vibration isolators with adjustable stiffness and transmissibility properties, making them suitable for a wide range of applications.

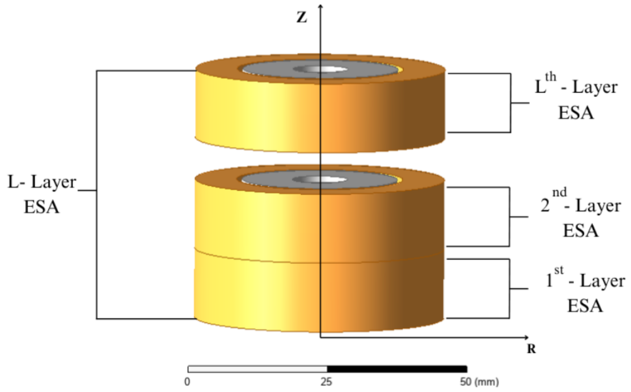

Figure 2.3: ESA at the equilibrium point

2.4.1 ESA Configurations

In an ESA system, the same current flows through the coils of all units. The clockwise current direction and the upward magnetization direction are considered positive. Thus, a unit with an upward magnetizing magnet can be represented by P and that with a downward magnetizing magnet by N. The arrangement of these units defines two primary configurations:

i **Unipolar Electromagnetic Spring Assembly (UESA):** In this configuration, all units have the same magnetization direction, either positive (P) or negative (N). Each sub-unit's magnetic field aligns in the same orientation, creating a uniform polarity across the assembly.

ii **Alternating Polarity Electromagnetic Spring Assembly (AESA):** This configuration alternates between positive (P) and negative (N) units, forming an arrangement with alternating magnetic polarities. The direction of the control current in the coils determines the unit's polarity. For instance, a clockwise current induces a positive (P) polarity, while an anticlockwise current results in a negative (N) polarity.

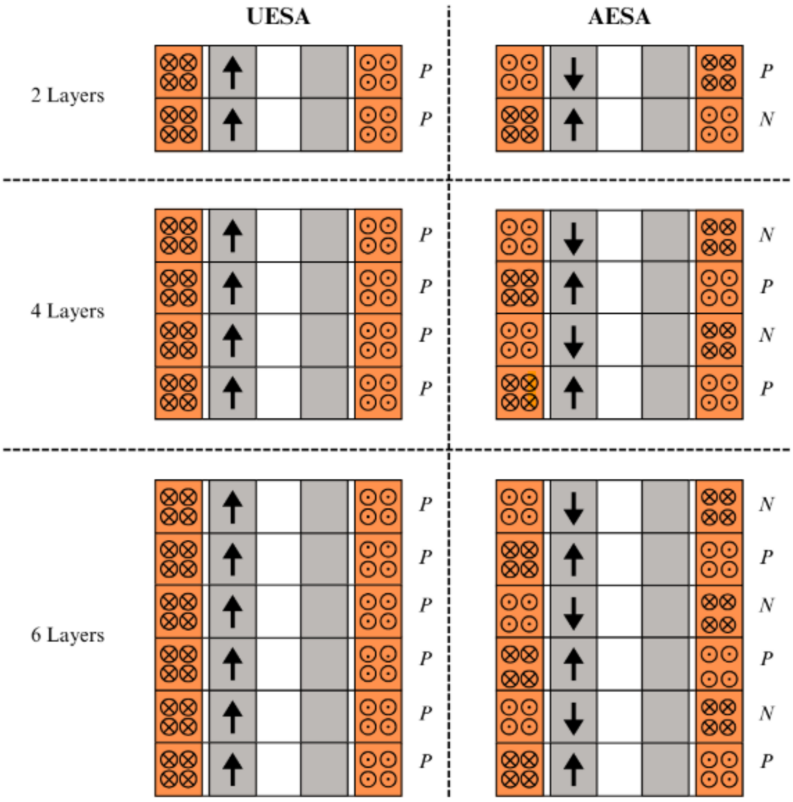

Figure 2.4: ESA configurations for negative stiffness generation.

2.5 Evaluation of Electromagnetic Force

2.5.1 Direct Analytical Method

The traditional (direct analytical) method for calculating the magnetic force between two planar coils is grounded in classic electromagnetic theory. It involves the use of integrals based on the magnetic vector potential $\vec{A}$. The magnetic field generated by one coil interacts with the current density and spatial configuration of the other, leading to the resultant force between them.

Using the vector potential $\vec{A}$ simplifies the calculation compared to working directly with the magnetic field $\vec{B}$. Instead of evaluating the complex interactions of $\vec{B}$ in three dimensions, this approach leverages $\vec{A}$, which inherently incorporates the coil geometry and current distribution.

However, computing the force on one coil due to the effect of another this way leads to complicated integrals. To that extent, we first consider the electromagnetic force exerted by a single filament of such a planar coil. Thus, a system of two concentric circular filaments (of the two coils) is considered.

A. Shiri and A. Shoulaie [3] derived the following equation for the force a ring 1 exerts on ring 2:

$$F_{21} = -a_z \frac{\mu_0 a b I_1 I_2 z}{2} \int_0^{2\pi} \frac{\sin\phi'}{[z^2 + a^2 + b^2 - 2ab\sin\phi']^{3/2}}\, d\phi' \qquad [3] \qquad (2.1)$$

Here, a and b are the radii of rings 1 and 2, respectively, and z is the axial distance between the two rings. This obtained force has no analytical solution, so the authors employed numerical integration methods to solve it. The variable ϕ' was replaced by $3\pi/ 2 + 2\ \theta$ to obtain an equation in terms of elliptic integrals.

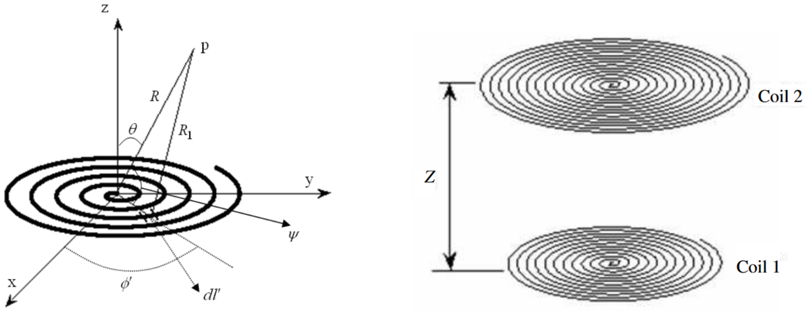

Figure 2.5: Calculation of vector magnetic potential of spiral coils in any given point P [3]

$$F_{21} = a_z \left(\frac{\mu_0 I_1 I_2 z k}{2\sqrt{ab}(1-k^2)} \right) \left[(1-k^2)K(k) - \left(1 - \frac{1}{2}k^2\right) E(k) \right] \qquad [3] \qquad (2.2)$$

In this equation, k is a constant coefficient whose value is given by the geometrical dimensions of the system:

$$k = \sqrt{\frac{4ab}{(a+b)^2 + z^2}} \qquad [3] \qquad (2.3)$$

K(k) and E(k) are the first and second-order elliptic integrals, respectively, which are defined as

$$K(k) = \int_0^{\frac{\pi}{2}} \frac{d\theta}{(1-k^2\sin^2\theta)^{1/2}} \qquad [3] \qquad (2.4)$$

$$E(k) = \int_0^{\frac{\pi}{2}} (1-k^2\sin^2\theta)^{1/2} d\theta \qquad [3] \qquad (2.5)$$

Elliptic integrals are fundamental to this problem because they mathematically represent the interaction between current loops with circular symmetry, accounting for the complex dependence of magnetic fields on geometry and position. Surface integrals would be theoretically equivalent, but are practically infeasible due to their multi-dimensional nature and lack of closed-form solutions. Additionally, numerical evaluations of these integrals (e.g., using tools like MATLAB, Mathematica, or Python libraries like scipy.special) allow precise calculation of forces and mutual inductance without resorting to computationally expensive direct integration.

By first describing the force interaction between two concentric circular filaments, the extrapolation of the forces to planar coils having multiple such filaments is possible. However, other simplifications and assumptions are made to make calculations easier. Most notable is the division of the coil into a rectangular mesh or filaments, which is discussed in the following section.

2.5.2 Filament Method

The filament method employs the discretization of planar coils into several segments called filaments. Essentially, a planar circular coil is represented by multiple filaments as specified by the mesh for the coil. It is to be noted that coil 1 is divided into $i \times j$ filaments (i segments in the radial direction and j in the axial direction), and coil 2 is divided into $k \times l$ filaments.

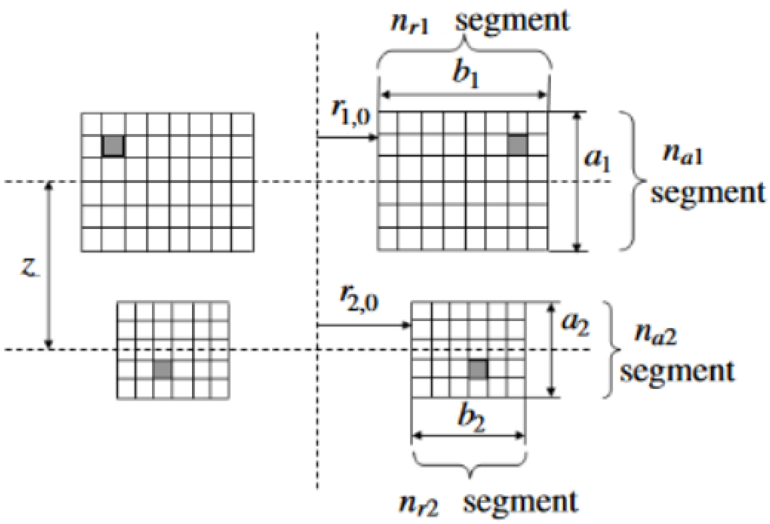

Figure 2.6: Division of the coils into different meshes to calculate the force between them. [3]

If I_1 and I_2 are the currents flowing through coils 1 and 2, the current through each filament is a proportion of the coil current.

$$i_1 = \frac{N_1 I_1}{n_{r1} \times n_{a1}}, \quad i_2 = \frac{N_2 I_2}{n_{r2} \times n_{a2}} \qquad [3] \tag{2.6}$$

The effective force between the coils is the sum of all forces between all the filaments of both coils.

$$F_{21} = \sum_{k=0}^{n_{r2}-1} \sum_{j=0}^{n_{r1}-1} \sum_{l=0}^{n_{a2}-1} \sum_{i=0}^{n_{a1}-1} f(k,j,l,i) \tag{2.7}$$

[3]
As introduced earlier, the equation for the force between two concentric filaments is given by

$$f(k,j,l,i) = a_z \left(\frac{\mu_0 i_1 i_2 z i' k'}{2\sqrt{r_k r_j}(1-k'^2)} \right) \left[(1-k'^2)K(k') - \left(1 - \frac{1}{2}k'^2\right) E(k') \right] \quad [3] \tag{2.8}$$

Where, $K(k')$ represents the elliptic integral of the first kind,

and $E(k')$ represents the elliptic integral of the second kind

The parameters involved in the above equation have also been defined as:

$$r_k = r_{2,0} + \left(\frac{1}{2} + k\right)\left(\frac{b_2}{n_{r2}}\right) \qquad [3] \tag{2.9}$$

$$r_j = r_{1,0} + \left(\frac{1}{2} + j\right)\left(\frac{b_1}{n_{r1}}\right) \qquad [3] \tag{2.10}$$

$$z_{il} = z - \left[\left(\frac{a_2}{2}\right) + \left(\frac{a_1}{2}\right)\right] + \left(\frac{1}{2} + i\right)\left(\frac{a_1}{n_{a1}}\right) + \left(\frac{1}{2} + l\right)\left(\frac{a_2}{n_{a2}}\right) \tag{2.11}$$

[3]

$$k' = \sqrt{\frac{4r_k r_l}{(r_k + r_l)^2 + z_{il}^2}} \qquad [3] \tag{2.12}$$

Here, r_k and r_j represent the radial distance of each mesh, z_{il} represents the distance between the i and l layer of the mesh The filament method is particularly well-suited for applying the findings of Robertson et al. [20] on the force equivalence of coaxial cylindrical magnets and thin coils. As an interpretation of their approach, a ring magnet is effectively modeled as two solenoids—an inner and an outer one—with opposing current directions. This representation simplifies the complex magnetic behavior, enabling the filament method to be applied to the equivalent system of two solenoids and a static coil.

If each equivalent solenoid of the magnet can be subdivided into a mesh of W elementary loops with the same current, we can write the following relation for the current flowing through them:

$$I_j^A = -I_j^B = \frac{J_j H}{\mu_0 W} \qquad [3] \tag{2.13}$$

Subsequently, the filament method can be utilized as before to determine the force between a permanent magnet, now represented by two equivalent coils and a planar coil.

2.5.3 Magnetostatic Solver in Ansys Maxwell

The magnetostatic solver in Ansys Maxwell calculates static magnetic fields in 2D or 3D, resulting from DC currents in conductors/coils and permanent magnets. It assumes no time-variation effects and models objects as stationary. The solver uses finite element analysis (FEA) to solve Maxwell's equations for magnetostatics:

Magnetic Field Intensity(H):

Governed by

$$\nabla \times \vec{H} = \vec{J} \tag{2.14}$$

$$\nabla \cdot \vec{B} = 0 \tag{2.15}$$

where B is the magnetic flux density, H is the magnetic field intensity, and J is the current density.

Material Relationships:

$$\vec{B} = \mu_0 \left(\vec{H} + \vec{M} \right) = \mu_0 \cdot \mu_r \cdot \vec{H} + \mu_0 \cdot \vec{M}_p \tag{2.16}$$

where μ depends on the material's properties and could be nonlinear (e.g., in permanent magnets or soft magnetic materials)

For nonlinear materials, the relationship between the magnetic fields H and B can exhibit isotropic or orthotropic behavior. In the case of anisotropic materials, the relative permeability μ_r is expressed as a tensor. This approach also accounts for nonlinearity in permanent magnets, including scenarios involving demagnetization conditions below the magnetic knee.
The solver relies on $B-H$ curves for the principal material directions to extract energy dependencies, facilitating the calculation of the nonlinear permeability tensor. This tensor is iteratively refined using the Newton-Raphson method:

$$\vec{B} = \vec{B}_0 + [\vec{\mu}] \cdot \left(\vec{H} - \vec{H}_0 \right) [\vec{\mu}] = \frac{\partial}{\partial \vec{H}} \vec{B} = [\Delta \vec{\mu}] + [\vec{\mu} \tag{2.17}$$

Where B_0 and H_0 are the previous field solution, is a general full tensor, and $[\mu]$ is given by the following:

$$\vec{\mu} = \begin{bmatrix} \mu_x & 0 & 0 \\ 0 & \mu_y & 0 \\ 0 & 0 & \mu_z \end{bmatrix} \tag{2.18}$$

with μ_x , μ_y , μ_z, taking into account the anisotropic effects of any laminations present in the model. The 3D magnetostatic solver considers the magnetic field H with the following components:

$$\vec{H} = \vec{H}_p + \nabla \varphi + \vec{H}_c \tag{2.19}$$

Here, ϕ is the magnetic scalar potential, H_p is a particular solution ensuring Ampere's law, and H_c accounts for permanent magnet contributions. The quadratic approximation for the scalar potential enables computational efficiency and stability while minimizing cancellation errors. Nonlinear problems are handled through iterative techniques with user-controlled accuracy. The solver supports boundary conditions for simulating devices immersed in external magnetic fields, ensuring that Maxwell's equations are satisfied across the solution domain.

CHAPTER 3

METHODOLOGY

To eventually design a vibration isolator with the electromagnetic spring as its core negative stiffness mechanism, a detailed design of the electromagnetic spring assembly (ESA) was conducted. A mathematical model was derived to predict the axial force, and thereby (negative) stiffness of the ESA, and this model was validated with simulations in Ansys Maxwell. Past research and studies pointed to the filament method as the mathematical model of choice [17], [21]. In the filament method, both the permanent magnet and coil windings are discretized into elementary filaments, and the magnetic forces between each filament pair are summed to yield the net axial force. The equations were implemented in Python, taking magnet and coil geometry, material properties, current, and assembly configuration as inputs to generate force–displacement and stiffness-displacement plots. These plots were used to select magnets, coils, and mechanical springs as they revealed the range of negative stiffness achievable with commercially available magnet grades and sizes. Based on market availability and ease of procurement, suitable components were then obtained for prototype fabrication and further experimentation.

An experimental setup was put in place to measure the axial force exerted on the magnets due to the current flowing in the coils at discrete displacement steps from the equilibrium. The magnets were mounted to and aligned with the shaft via collars and linear bearings, transmitting any motion and force experienced through a coupler to a load cell. The load cell output was amplified by an HX711 module and read by an Arduino Uno connected to a PC. Static force readings were taken by moving the magnets in fixed increments from the equilibrium position, passing current through the coils, and recording the resulting force. This procedure was repeated for different numbers of ESA units and configurations (AESA and UESA) to generate practical force–displacement data and derive the corresponding negative stiffness.

Simultaneously, the vibration isolator prototype was modeled in SolidWorks. Dimensions of key components — magnets, mechanical spring, and copper coils — were based on availability and performance requirements from the analytical models. To realize the isolator, a mechanical spring with positive stiffness closely countering the ESA's negative stiffness was preferred. However, because the magnet grade limited the attainable negative stiffness, the quasi-zero-stiffness (QZS) requirement was relaxed, and a lower-stiffness spring that fit the geometric constraints was used. The isolator body, collars, and bearing housings were 3D-printed from PLA. A prototype shake table was built from plywood for experimental testing.

The isolator's performance was verified by subjecting the prototype to sinusoidal vibrations of known amplitude and frequency using a vibration exciter. Payload acceleration, measured by an accelerometer, was captured through a charge amplifier and NI myDAQ. In LabVIEW, filtering and calibration yielded real-time acceleration data. As coil current increased, transmitted acceleration dropped noticeably, confirming tunable vibration suppression. Due to time and equipment constraints, full transmissibility curves and an exact natural-frequency estimate were not obtained.

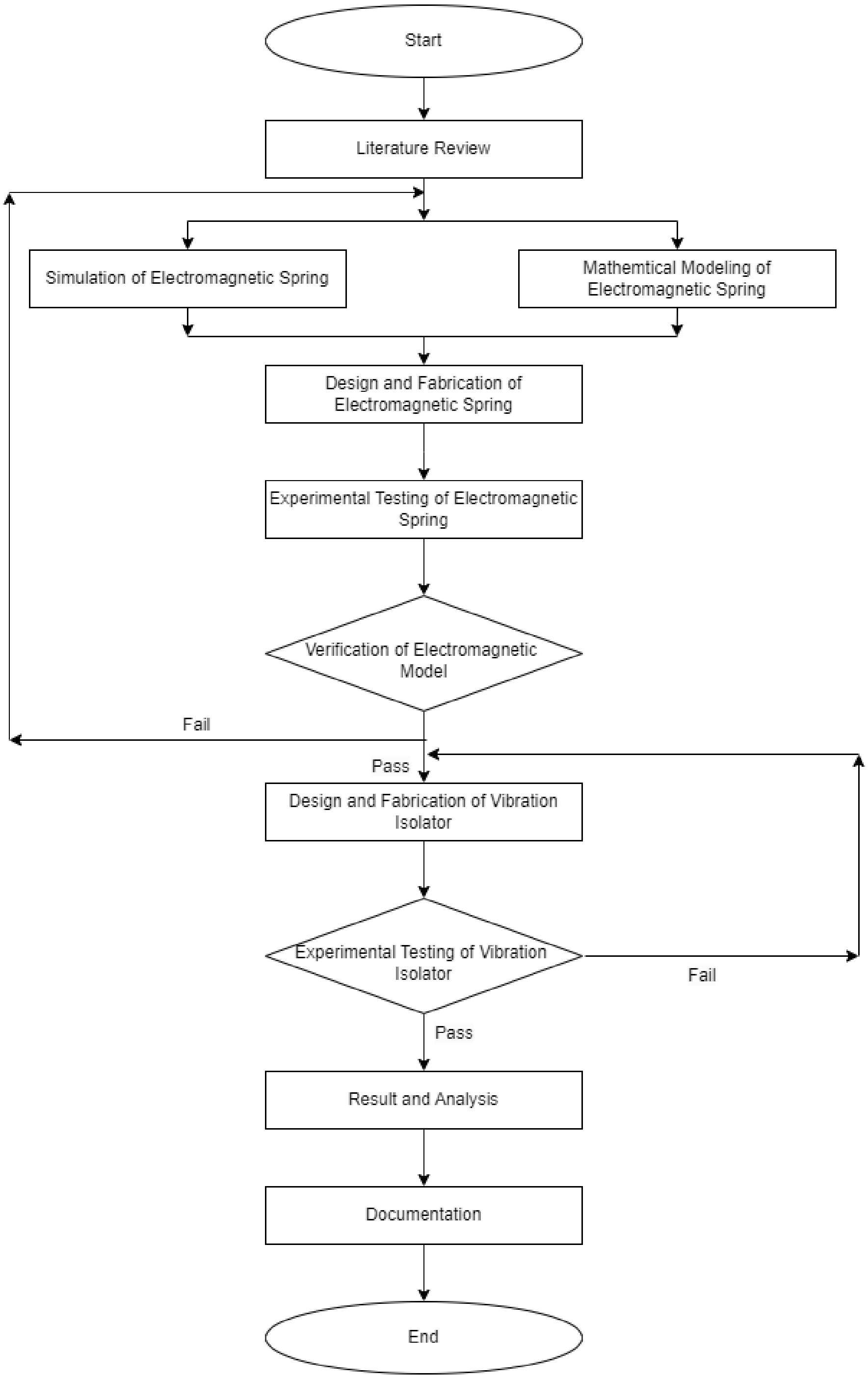

Figure 3.1: Methodology Flowchart

CHAPTER 4

DESIGN, SIMULATION, AND EXPERIMENTATAL SETUP

4.1 Mathematical Modeling

The examination of the negative stiffness characteristics of the electromagnetic spring assembly begins with the calculation of the electromagnetic force resulting from the interaction between the electromagnet copper coils and the neodymium permanent magnets.

Based on the availability of materials and specifications, the dimensions of the magnet and coil are as follows:

Table 4.1: Dimensions of Magnet and Coil

Parameter	Remarks	Unit	Value
J	Magnetic permeability	T	0.345
H	Height of unit ESA	mm	12.5
d_m	Inner diameter of permanent magnet	mm	10
D_m	Outer diameter of permanent magnet	mm	28
d_c	Inner diameter of electric coil	mm	30
D_c	Outer diameter of electromagnetic coil	mm	45
i	-	-	25
j	-	-	15
k	-	-	50

The filament method is a numerical approach designed to calculate the electromagnetic force between coils and magnets with precision and efficiency. It is especially useful in systems where magnetic components interact over varying distances and currents, such as electromagnetic springs in vibration isolation devices.

In this approach, each coil or magnet is divided into smaller segments called filaments, which act as unit coils. Each filament carries a fraction of the total current, proportional to the coil's overall current.

This discretization enables modeling the magnetic interaction at a granular level, where the forces between all filament pairs are computed and summed to determine the total force. The calculation of force between filaments is calculated using Eq.(2.8)

4.1.1 Geometrical Configuration of the System

In the system, the coil is denoted as W_x in the x-th layer, and the magnet is labeled as M_y in the y-th layer. The inner radii of the magnet and coil are represented by R_{mi} and R_{ci}, respectively, while the outer radii are R_{mo} and R_{co}. The axial height of both components is denoted by H. The axial position of the x-th layer is given by:

$$Z_x = Z_1 + (x-1)H, \tag{4.1}$$

with the position of the static coil at Z_x and the magnet at $Z_x + D$, where D is the offset between the coil and magnet in the axial direction.

4.1.2 Magnetic Field Superposition and Equivalent Solenoids

The magnet is modeled as two thin-walled solenoids, one internal and one external, with reverse currents on the cylindrical surfaces, denoted as B_y and A_y, respectively. By applying the principle of magnetic field superposition and Ampere's current model, the ring magnet can be equivalently modeled by these solenoids. Each equivalent solenoid can be subdivided into a mesh of L elementary loops with the same current, satisfying the following relationship:

$$I_y^A = -I_y^B = \frac{J_y H}{\mu_0 W} \tag{4.2}$$

The polarization of the l-th loop is represented by J_l, and the vacuum permeability is denoted by μ_0.

4.1.3 Coil Geometry

The elementary loop located at the internal equivalent solenoid of magnet M_y is denoted by B_l^y, and the one at the external solenoid by A_l^y, where $l = 1, 2, \ldots, L$. The position of these loops can be defined in a cylindrical coordinate system as follows:

$$Z_l^{Ay} = Z_l^{By} = Z_y + D + \frac{2l-1}{2L}H, R^{Ay} = R_{mo} \tag{4.3}$$

and

$$R^{By} = R_{mi}$$

The static coil W_x consists of J axial layers and I radial layers, resulting in a total of $I \times J$ turns, each carrying a current I_x^W. The turns are uniformly distributed, with each turn denoted as $W_{i,j}^x$, where $i = 1, 2, \ldots, I$ and $j = 1, 2, \ldots, J$. The z-coordinate and radius of each coil turn are defined in a cylindrical coordinate system as:

$$Z_{i,j}^{Wx} = Z_x + \frac{2u-1}{2U}H, \text{ and } R_{i,j}^{Wx} = R_{ci} + \frac{2v-1}{V}(R_{co} - R_{ci}) \tag{4.4}$$

4.1.4 Maxwell's Coil Interaction

Each turn of the static coil $W^x_{i,j}$, and an elementary loop of the internal solenoid B^y_l form a Maxwell's coil. The electromagnetic force between these pairs can be calculated using the standard Maxwell's coil force equation [insert equation here]. The force between the equivalent internal solenoid B^y and the static coil W^x is determined by adding the interaction forces between all pairs of Maxwell's coils.

$$\begin{aligned} F^{Wx/By}_{i,j/l}\left(I^W_x\right) &= \frac{\mu_0 I^W_x I^B_y \left(Z^{By}_l - Z^{Wx}_{i,j}\right) K^{Wx/By}_{i,j/l}}{4\sqrt{R^{Wx}_{i,j} R^{By}_l}} \left[2K\left(K^{Wx/By}_{i,j/l}\right) - \frac{2-\left(K^{Wx/By}_{i,j/l}\right)^2}{1-\left(K^{Wx/By}_{i,j/l}\right)^2} E\left(K^{Wx/By}_{i,j/l}\right) \right] \\ &= I^C_x F^{Wx/By}_{i,j/l} \end{aligned}$$

[19]

where

$$\left(K^{Wx/By}_{i,j/l}\right)^2 = \frac{4R^{Wx}_{i,j} R^{By}_l}{\left(R^{Wx}_{i,j} + R^{By}_l\right)^2 + \left(Z^{By}_l - Z^{Wx}_{i,j}\right)^2}. \tag{4.5}$$

4.1.5 Force Calculation for Internal and External Solenoids

The total force between the static coil W^x and the ring magnet can be split into two components: the force between the internal equivalent solenoid By and the coil, and the force between the external equivalent solenoid A^y and the coil. The interaction force for each component is calculated by summing the forces between all the filament pairs. Specifically, the force between the internal solenoid and the static coil is given by:

$$F^{W/B}_{x/y}\left(I^W_x\right) = \sum_{l=1}^{L} \sum_{j=1}^{J} \sum_{i=1}^{I} F^{Wx/By}_{i,j/l}\left(I^W_x\right) = I^W_x \sum_{l=1}^{L} \sum_{j=1}^{J} \sum_{i=1}^{I} F^{Wx/By}_{i,j/l}. \qquad [19] \tag{4.6}$$

Similarly, the force between the external solenoid and the static coil is:

$$F^{W/A}_{x/y}\left(I^W_x\right) = \sum_{l=1}^{L} \sum_{j=1}^{J} \sum_{i=1}^{I} F^{Wx/Ay}_{i,j/l}\left(I^W_x\right) = I^W_x \sum_{l=1}^{L} \sum_{j=1}^{J} \sum_{i=1}^{I} F^{Wx/Ay}_{i,j/l}. \qquad [19] \tag{4.7}$$

4.1.6 Total Electromagnetic Force

The total electromagnetic force between the magnet and the coil is the sum of the internal and external force components:

$$F_{x/y}^{W/M} = F_{x/y}^{W/A}\left(I_x^W\right) + F_{x/y}^{W/B}\left(I_x^W\right) = I_x^W\left(\sum_{l=1}^{L}\sum_{j=1}^{J}\sum_{i=1}^{I} F_{i,j/l}^{Wx/By} + \sum_{l=1}^{L}\sum_{j=1}^{J}\sum_{i=1}^{I} F_{i,j/l}^{Wx/Ay}\right) \quad [19] \tag{4.8}$$

4.1.7 Extension to Multiple Magnets and Coils

The analytical model can be extended to calculate the electromagnetic force between multiple magnets and coils. Using the $1M1C$ (1 Magnet, 1 Coil) model, the force between N magnets and N coils in an Electromagnetic Spring Assembly (ESA) can be computed by summing the individual interaction forces between each coil and magnet pair.

$$F_e^{W/M}(\vec{r}) = \sum_{j=1}^{N}\sum_{l=1}^{N} F_{x,y}^{W/M}\left(I_x^W\right) = I_c \sum_{j=1}^{L}\sum_{l=1}^{L} F_{x,y}^{W/M} \qquad [19] \tag{4.9}$$

4.1.8 Stiffness Calculation

The axial stiffness of the ESA can be obtained as the derivative of the electromagnetic force with respect to the relative axial displacement D as follows:

$$K\left(\vec{I^W}\right) = -\frac{dF_e^{W/M}\left(\vec{I^W}\right)}{dD} \qquad [19] \tag{4.10}$$

4.2 Simulations in ANSYS Maxwell

4.2.1 Geometry & Material Definition

The model represents a coaxial configuration of a Neodymium ring magnet and a current-carrying copper winding of the same height. Multiple models with varying numbers of individual units were created based on the dimensions stated earlier. The primary focus of the simulations is to study the electromagnetic forces developed on the ring magnet(s), which are predominantly axial (along the Z-direction) in nature.

The magnet's position along the Z-axis is not fixed due to the force interaction between the magnetic field of the ring magnet and the electromagnetic field generated by the current-carrying conductor. By defining a variable origin_ z, the displacement of the magnet can be dynamically accommodated during the simulation, reflecting a more realistic representation of the physical system where the magnet's position is adjusted based on the force it experiences.

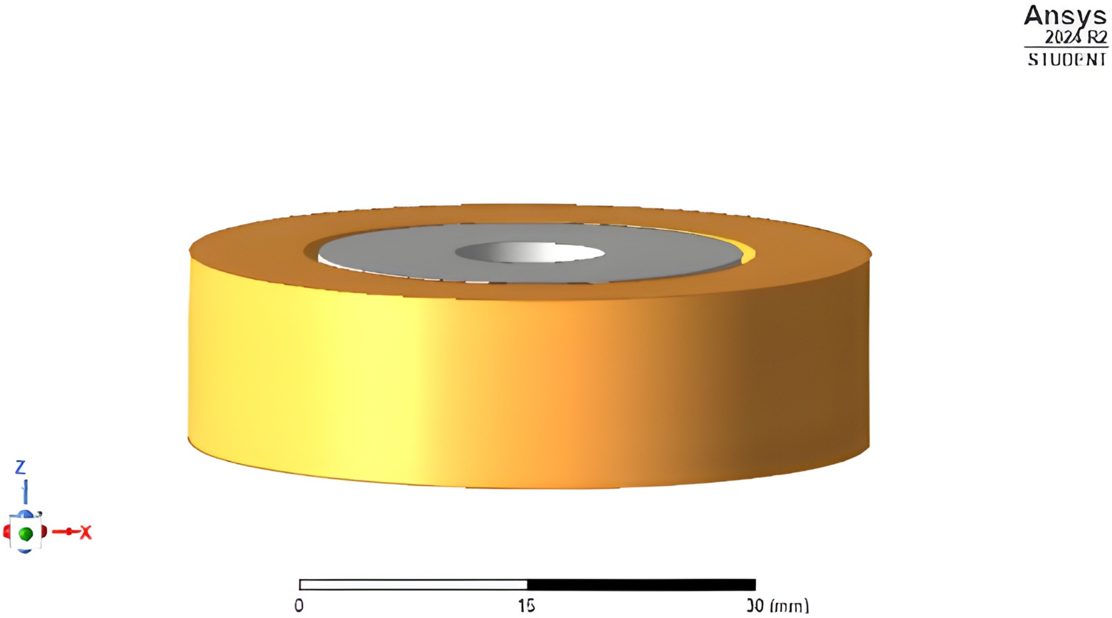

Figure 4.1: Model of a single ESA unit

A surrounding simulation region with 100% padding ensures that the magnetic fields can develop freely without interference from boundary conditions. The medium is set to air to eliminate environmental influences, ensuring that the results reflect only the interaction between the magnet and the conductor.

Table 4.2: Material properties of Neodymium magnet and Copper coil winding

Material	Property	Value	Unit
Neodymium N35 grade permanent magnet	Magnetic Permeability (μ)	1.05	-
	Permanent Magnetization	0.345	T
	Magnetic Field Strength (H_c)	-261468.835	A/m
Copper coil winding	Relative Magnetic Permeability (μ_r)	0.999991	-
	Bulk Conductivity	58,000,000	S/m

4.2.2 Excitation & Boundary Conditions

A rectangular cross-section is chosen for the conductor as per the geometry. Across multiple simulations, the current supplied to the coil is varied between 3 A and 5 A to observe how the current impacts the magnetic force. Based on the nominal diameter of a winding (1.5 mm), the number of conductor coils associated with a rectangular cross-section of the winding is set to be 30 coils. For setups involving multiple coils, the number of conductors is multiplied accordingly.

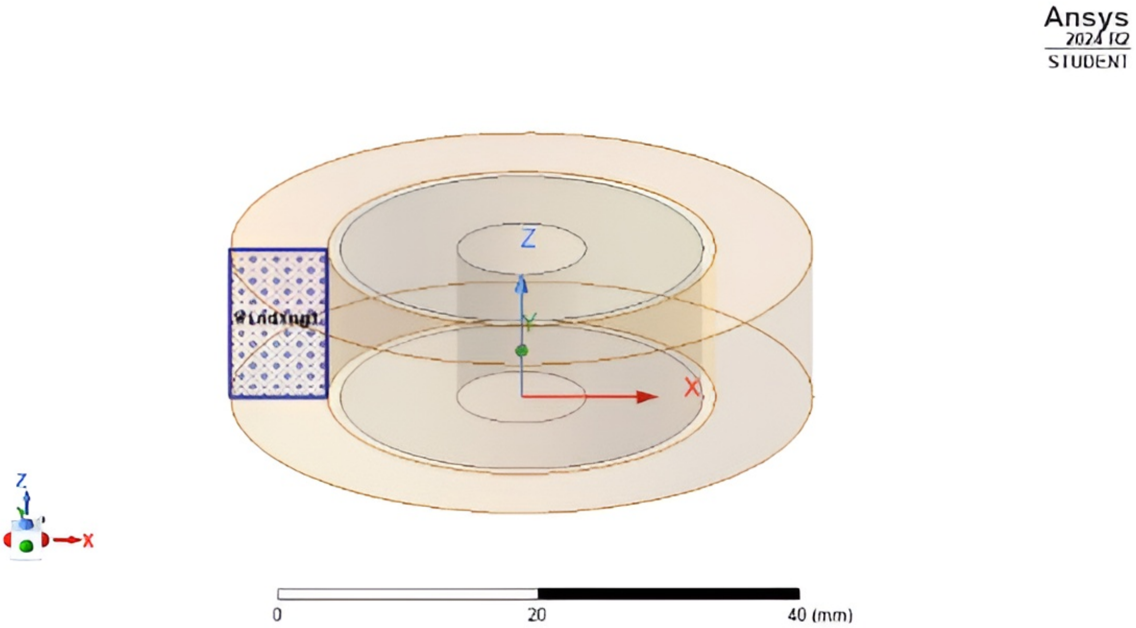

Figure 4.2: Conductor in a Rectangular Section of the Coil Winding

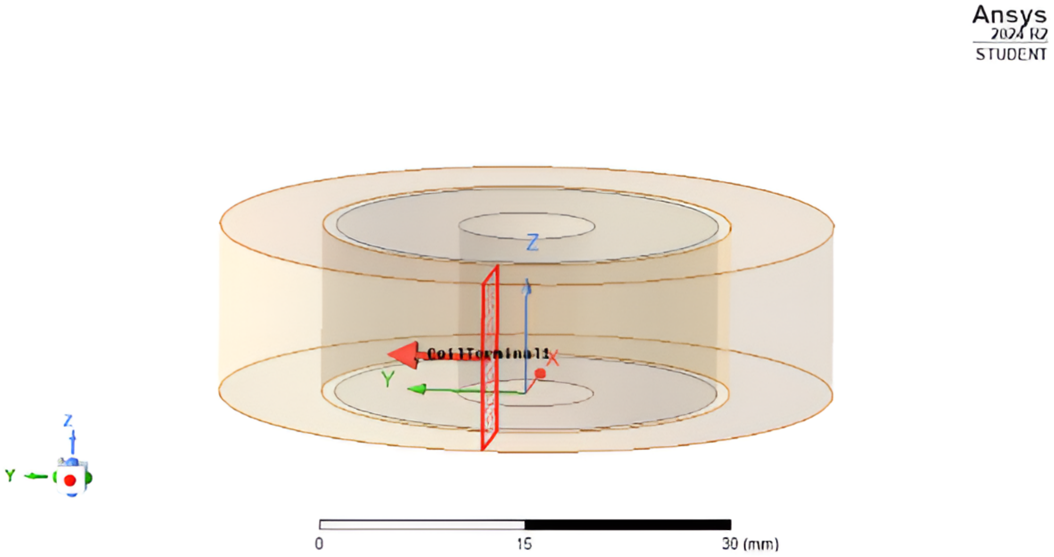

Figure 4.3: Direction of Current Specified for the Winding

The force on the magnet is computed using the virtual force method. Since the Lorentz force does not compute the correct force on objects that are assigned materials with a relative permeability greater than one (that is, materials where $\mu \neq \mu_0$), the force type is chosen to be virtual.

The default mesh settings is employed. The Auto Mesh Method is employed to create an initial mesh that adapts to the geometry of the magnet and coil.

4.2.3 Solver Configuration

Magnetostatic solver is the solver of choice. The solver settings are by default. The origin _ z variable is used as a sweep parameter in the analysis. By systematically varying the magnet's Z-coordinate, the force acting on the magnet at different axial positions can be calculated.

4.2.4 Force Computation

The force on the magnet is calculated along the Z-axis using the Optimetrics module, which provides precise results for the axial force at different current and displacement values.

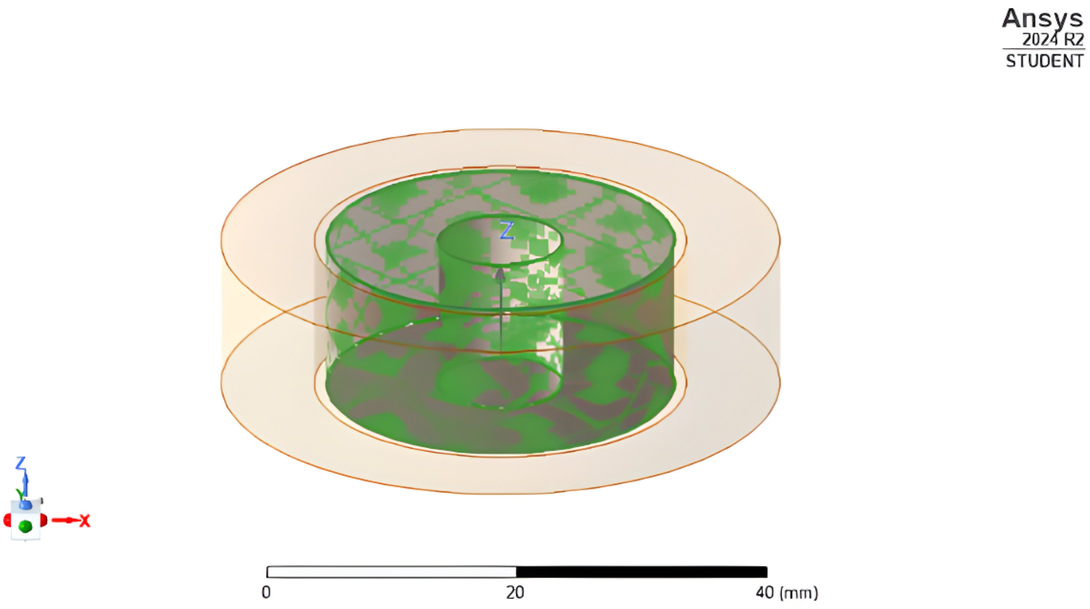

Figure 4.4: Application of Virtual Forces on the Ring Magnet

4.2.5 Summary of Simulation in Ansys Maxwell

Table 4.3: Simulation Setup in ANSYS Maxwell

Category	**Details**
Model	Configuration: Permanent magnet (Neodymium ring) and coaxial current-carrying conductor. Varying in the number of units. Region Setup: 100% padding along the x and y axes, 200% padding along the z-axis; Medium: Air.
Material Properties	Neodymium Ring Magnet: Permeability (μ) = 1.05, Permanent Magnetization (Mp) = 0.345 T. Coil Winding: Relative Permeability = Defined, Bulk Conductivity = Defined.
Excitation Setup	Winding Type: Stranded. Current Range: 3 A to 4.5 A. Coil Terminal Excitation: 30 turns per static coil.
Parameter: Force on magnet(s)	Force Type: Virtual
Mesh Settings	Initial Mesh Method: Auto. Curved Surface Meshing: Fine resolution. Refinement per Pass: 30%. Minimum Passes: 2, Maximum Passes: 10.
Solver Setup	Minimum Convergence Passes: 1. Nonlinear Residual: 0.0001.
Optimetric	Parametric setup: Variable - origin_z, Linear step from -40 mm to +40 mm, step = 2 mm.
Result Analysis	Parameter: Force along z axis, Primary Sweep: origin_z.

4.3 Prototype Design and Fabrication

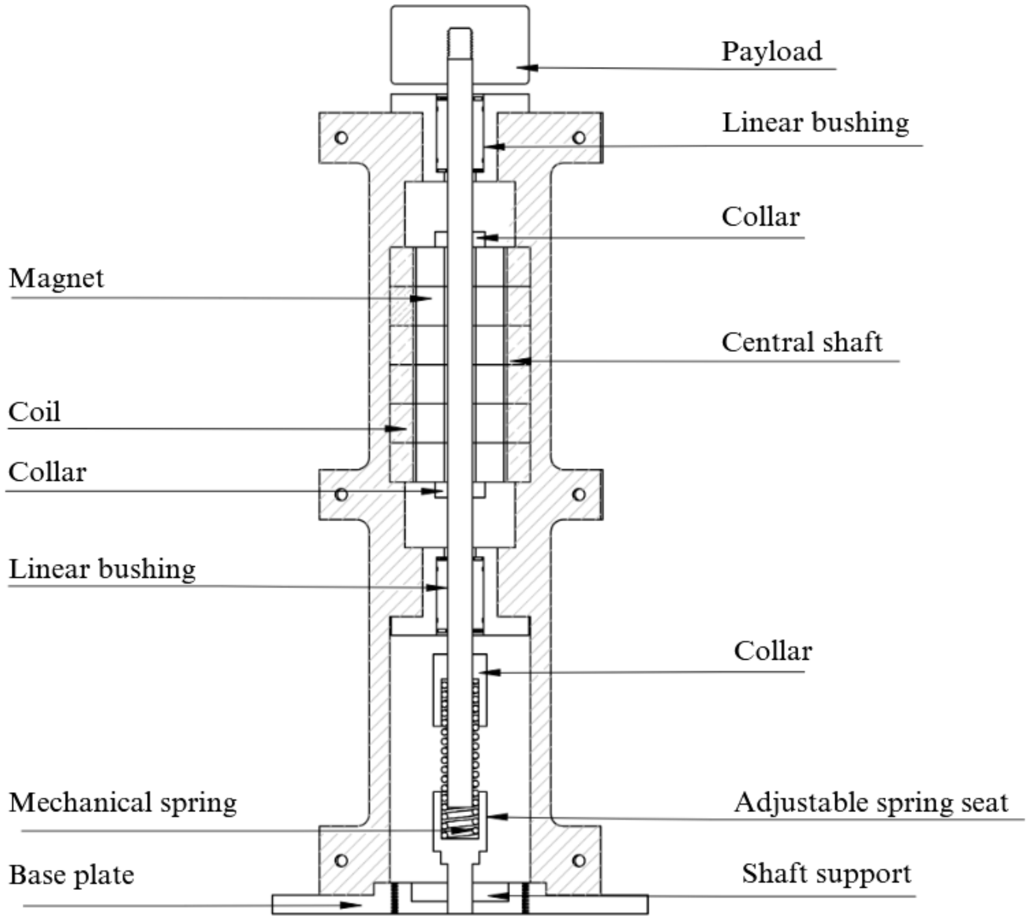

Figure 4.5: Cross-Sectional View of the Vibration Isolator Design

The vibration isolator was designed with three main objectives in mind: achieving effective negative stiffness, ensuring a compact and cost-effective design, and meeting the specific demands of vibration isolation. To achieve negative stiffness, the design incorporated an Electromagnetic Spring Assembly (ESA) configuration, which provided the required performance for effective vibration isolation. The focus on compactness ensured the isolator could be easily integrated into various systems, while the use of affordable materials and efficient fabrication methods balanced cost and performance. Additionally, the components were carefully selected to meet the requirements of tunable stiffness, stability, and smooth operation under different operating conditions.

4.3.1 Selection of Key Components

Mechanical Spring Selection

The mechanical spring plays a key role in balancing the system by providing positive stiffness. Its stiffness was carefully designed to slightly exceed the maximum negative stiffness produced by the ESA, ensuring stability and preventing excessive deflection under load. By complementing the ESA, the spring enhances the isolator's vibration reduction capabilities, enabling precise and reliable isolation performance.

Magnet Selection

We chose Neodymium magnets for their exceptional magnetic strength, compact size, and excellent strength-to-size ratio, which are critical for achieving the desired negative stiffness in the ESA. While cobalt ferrite magnets were considered for their lower cost, their weaker magnetic properties made them unsuitable for this application. Similarly, Samarium-Cobalt (SmCo) magnets offered similar performance but were excluded due to their significantly higher cost compared to Neodymium magnets. After evaluating market availability and design requirements, we selected Neodymium magnets with a 10 mm internal diameter and a 28 *mm* external diameter, striking a balance between practicality and performance.

Coil Selection

We used copper wire with a diameter of SWG 16 rating to construct the coils. The dimensions and number of turns were planned to create a strong magnetic field and align precisely with the magnets. To ensure stability and durability during operation, the coils were firmly glued to the inner walls of the isolator housing.

Vibration Exciter

The exciter functions as the main source of vibration, generating motion in the shaker table through the use of a push rod, which is then transmitted to the shaft. The exciter to be used is B&K Type 4809, with a design frequency range as low as 10 Hz.

4.3.2 Design of Structural Components

Isolator Body

The isolator body is the central housing for all components. It is designed to provide structural support while accommodating the magnetic and mechanical elements of the system. A PLA filament based 3D printed body was chosen for its lightweight nature, cost-effectiveness, and low magnetic permeability. Variable infills were ensured for different parts based on their specific placement.

Shaft and Collars

The shaft acts as the core structural component, housing the magnets and the mechanical spring. A stainless steel shaft of diameter 8 mm was selected for its strength, resistance to deformation, and compatibility with the magnetic system. Shaft collars were made of nylon to avoid interference with the magnets and were used to secure the magnets in place, ensuring stability under dynamic conditions.

Bushing

3D-printed bushings that housed individual linear bearings were fabricated. For smooth vertical motion and alignment, linear bearings of appropriate size were integrated into the design, minimizing friction and ensuring reliable performance during operation.

Shake Table

To transfer the vibration from the vibration exciter to the isolator body and payload, a shake table is fabricated. Plywood was the material of choice due to its availability over aluminum alternatives. Support springs are used to suspend the 16 kg table; each support spring's stiffness (k) will be set at 5.57 kN/m, producing a natural frequency of 5.9 Hz. Four linear bushings are used to guide the table's movement, which is only vertical. A thin stainless steel push rod is used to excite the shaking table's vibration using the exciter, which is fixed to the frame.

4.4 Experimental Testing

4.4.1 Axial Force Measurement of ESA Units

To measure the electromagnetic force between the electric coils and permanent magnets, the setup was placed horizontally on a table. The electromagnet assembly is positioned on the left, with the permanent magnet attached to and aligned with a stainless steel shaft. A load cell measures the force along the shaft and is connected to the shaft via a custom 3D-printed coupler. On the opposite end, the load cell is fixed to a movable platform. A dial indicator is used to measure the displacement of the magnets from the fixed equilibrium position. This setup ensures proper alignment and consistent contact for accurate force-displacement measurements.

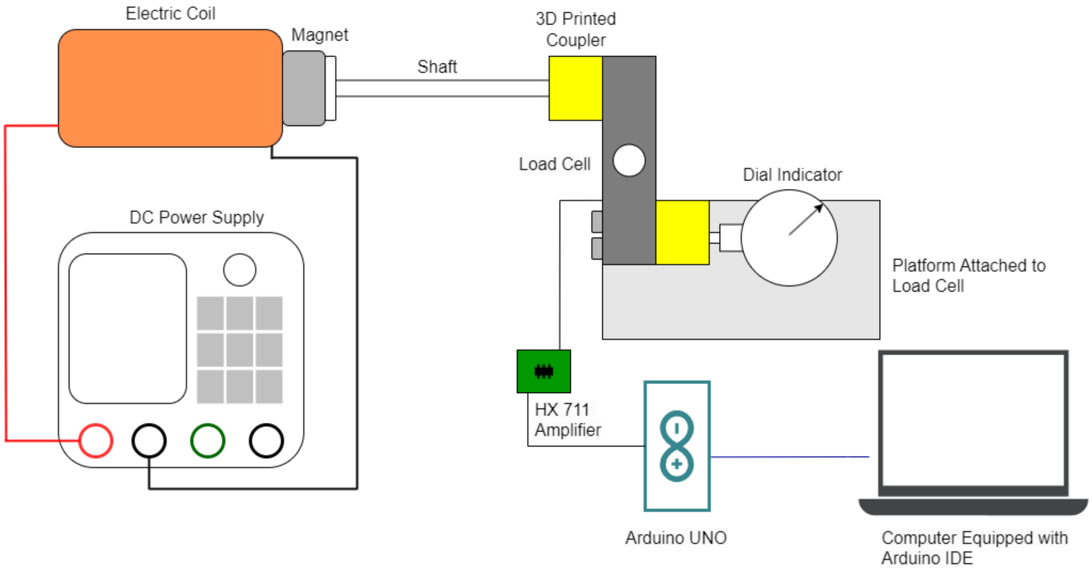

Figure 4.6: Schematic for Axial Force Measurement

Initial attempts to made to measure the force dynamically by continuously adjusting the magnet's position with a linear actuator. However, the force generated by the electromagnet-magnet interaction proved to be impulsive and jerky, which caused unintended displacement of both the shaft and the magnet and resulted in inconsistent data.

To address this issue, a static measurement approach was adopted. Instead of continuously moving the magnet(s), they were positioned at fixed distances from the coil in 2 *mm* increments, ensuring more stable and accurate force readings. The load cell, mounted with the custom 3D-printed parts, was connected to an HX711 amplifier and an Arduino UNO for data acquisition. Using this setup, forces were measured for both the UESA and AESA configurations. The results from this static approach closely matched our analytical models, confirming the accuracy of our analytical model.

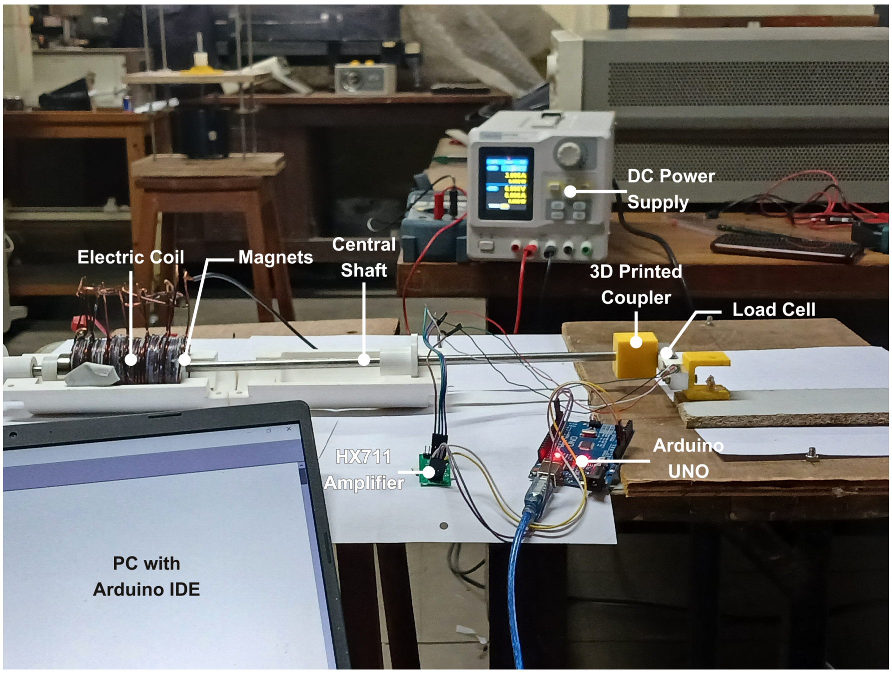

Figure 4.7: Experimental Setup for Measuring Axial Force of Electromagnetic Spring

4.4.2 Vibration Isolation Evaluation

Sensor Calibration

1. **Charge-amplifier calibration (built-in test source)**

   Before acquiring acceleration data, all connected devices must be calibrated. The Type 2635 charge amplifier (Fig. 4.8) converts the small charge signals from the accelerometer into voltage output. This output can be viewed on an oscilloscope or acquired using myDAQ.

   

   Figure 4.8: Front Panel of Charge Amplifier 2635

   To verify the amplifier's reliability, its internal test source generates a 160 Hz (1000 rad/s) sinusoidal signal when the REF push button is pressed. This signal is applied to the input stage and adjusted to a test voltage level of 1 V_{rms} at the OUTPUT socket. The output voltage is verified using an oscilloscope and myDAQ.

2. **Accelerometer calibration (handheld calibrator)**

   he Type 4371 accelerometer is calibrated using a handheld vibration reference, the B&K Type 4294. This device provides a standard acceleration level of 10 m/s^2 RMS (±3%) at 159.2 Hz (1000 rad/s). It also allows for velocity and displacement calibration at 10 mm/s and 10 μm, respectively.

Figure 4.9: Calibrator Type 4294

> The accelerometer is mounted on the calibrator using a 10-32 UNF stud. The reference signal ensures accurate adjustment of the measuring instrumentation to the standard acceleration level.

Experimental Setup for Acceleration Measurement

To generate controlled vibrations, the Brüel & Kjær Type 4809 vibration exciter was used. This device converts an electrical signal into a mechanical force of up to 44.5 N, with a maximum displacement of 8 mm. Operating within a frequency range of 20 Hz to 20 kHz, the exciter is designed to minimize unwanted lateral motion, ensuring that the applied vibrations remain purely axial.

The vibration response is measured using a high-precision Brüel & Kjær Type 4371 accelerometer, which has a charge sensitivity of 0.9950 $pC/(m/s^2)$. This high sensitivity enables the detection of even subtle vibrations. However, because the accelerometer outputs charge in pC, a Brüel & Kjær Type 2635 charge amplifier was used to convert it into a stable voltage signal suitable for data acquisition.

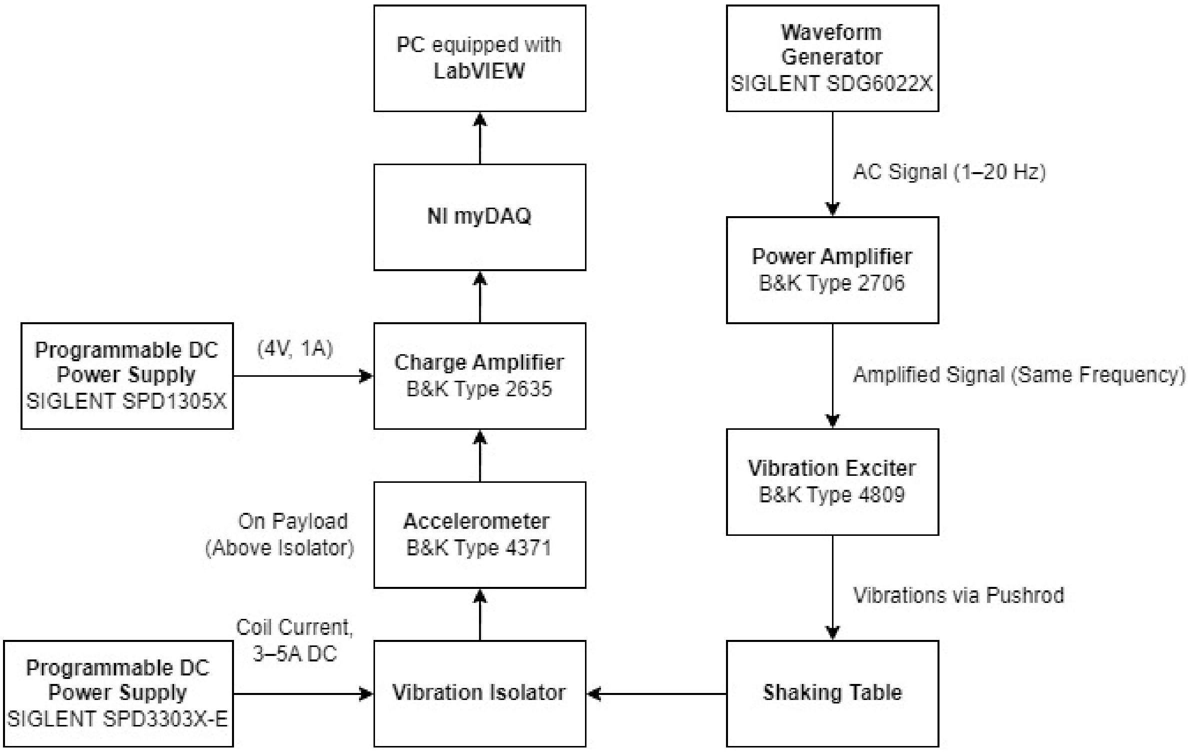

Figure 4.10: Schematic of Experimental Setup for acquiring acceleration data

The charge amplifier is carefully configured to ensure accurate signal processing. After powering it via its internal battery, the appropriate sensitivity range of either 0–1 $pC/(m/s)$ or 1–11 $pC/(m/s)$ was selected to match the accelerometer's output. To minimize electrical interference, any unused input was shielded, and the conditioning knob was adjusted to properly scale the signal. Additionally, the upper frequency limit was set just beyond our highest frequency of interest to filter out unnecessary noise.

For real-time data acquisition, NI myDAQ was used in conjunction with LabVIEW Community Edition. A custom LabVIEW VI was developed to continuously capture the analog voltage signal from the charge amplifier. The setup includes a DAQ Assistant Express VI, which was configured to define key parameters such as the sampling rate, number of samples, and timeout period.

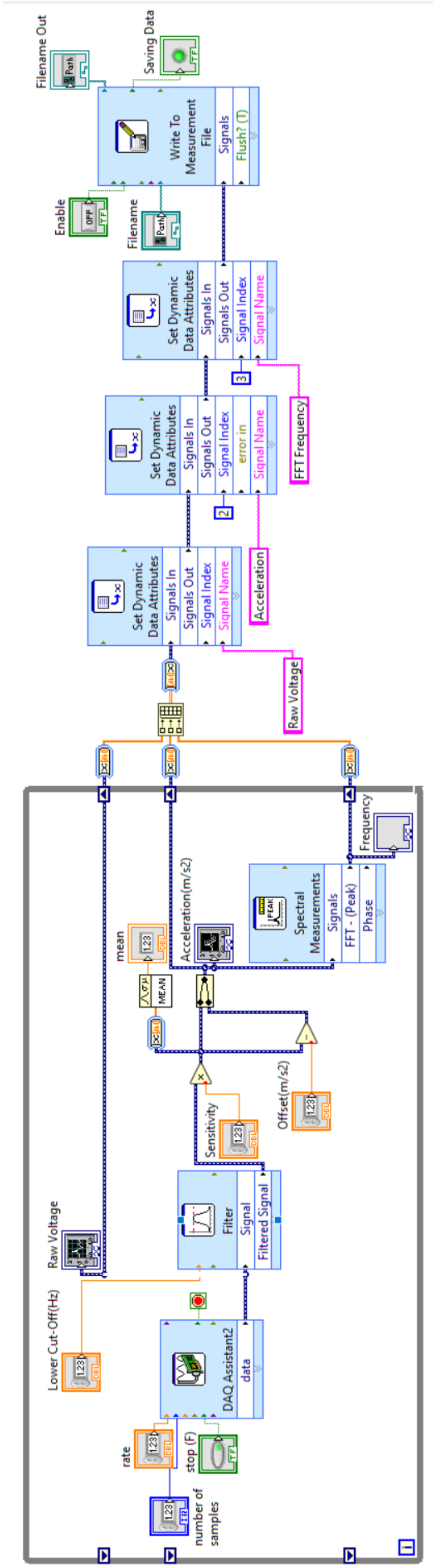

Figure 4.11: LabVIEW Block Diagram for Data Acquisition

These parameters could be easily adjusted via numeric controls on the LabVIEW front panel, allowing flexibility in data collection. The captured voltage signal followed two processing paths: one retained the raw voltage signal from the accelerometer, while the other applied a calibration factor to convert it into acceleration values (m/s²).

A 4th-order Butterworth low-pass filter with a 30 Hz cutoff effectively removed noise from the incoming accelerometer signal. The signals were properly labeled before being logged with time-stamped measurements for post-experiment analysis. This setup enabled a direct comparison between acceleration data before and after the isolator was activated, providing a quantitative assessment of its vibration-damping performance.

Procedure

Building on the detailed setup described earlier, the experiment aimed to quantify the vibration isolator's damping performance. To ensure stable and precise operation, two Siglent DC power supplies (SPD 3303X-E and SPD 1305X) were used - one dedicated to powering the charge amplifier and the other supplying current to the static coils of the isolator.

A single Brüel & Kjær Type 4371 accelerometer was placed on top of a payload (mass 400g), which itself was atop the vibration isolator. The accelerometer was mounted via a magnetic attachment provided by B&K. By comparing acceleration data recorded before and after the isolator was activated, the isolator's effectiveness in reducing vibrations was measured. The difference in these readings provided a direct measure of the isolator's performance.

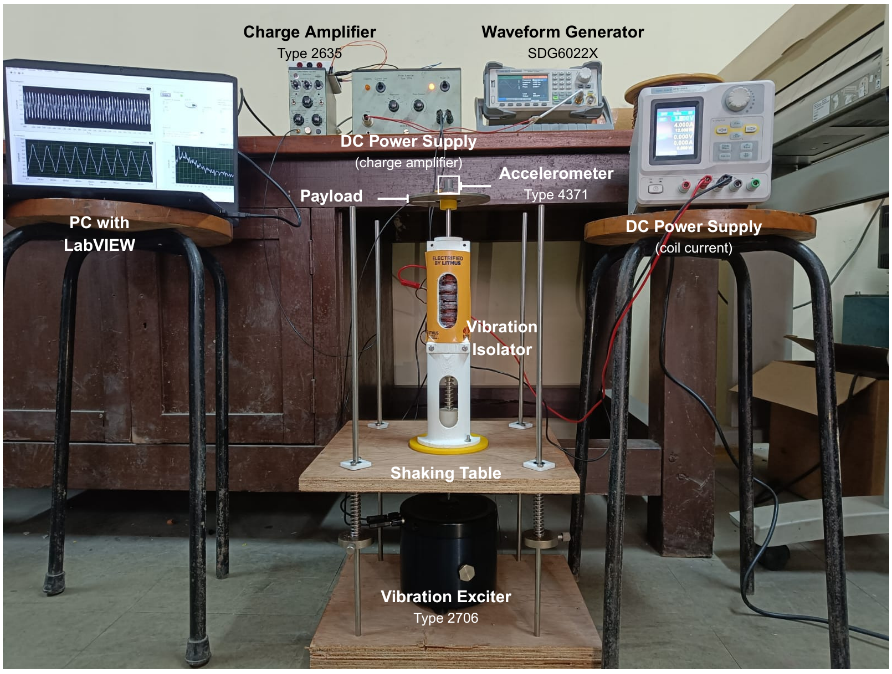

Figure 4.12: Experimental Setup for Acceleration Measurement

Since the Type 4371 accelerometer generated extremely small charge signals (approximately 0.995 pC/(m/s^2)), the charge amplifier was used to convert them into a usable voltage signal. The amplifier was set to the 0 to 1 pC/(m/s^2) range, and the conditioning knob was carefully adjusted to ensure precise signal scaling. The amplified voltage output was then sent to the NI myDAQ system through the Analog Voltage In 0 channel. To prevent signal clipping and keep the voltage within the -10 V to +10 V range, the gain control knob (adjustable from 0.1 to 1000 mV/unit) was fine-tuned and configured the ACC.-VEL.-DISPL. switch to match the measurement requirements, setting the output to 1 m/s^2 with a minimum frequency of 0.2 Hz.

The DAQ Assistant continuously captured the raw analog voltage input, and using the VI, both the raw voltage and corresponding acceleration data were logged into an Excel file for easy post-processing.

Before activation of the isolator, i.e., sending current to the copper coils, the system exhibited higher vibration levels. While after activation, the ESA-based isolator effectively isolated the vibrations, confirming its performance.

CHAPTER 5

RESULTS AND DISCUSSION

5.1 Force and Stiffness Characteristics of ESA

The force exerted due to the interaction between the magnetic fields of the permanent magnets and the electromagnetic coil was evaluated using three methods:

1. Mathematical modeling with the filament method.
2. Simulation in Ansys Maxwell.
3. Experimental validation using a load cell.

The average error between the mathematical model and simulation results across multiple configurations is 16.4%. The mathematical model deviates from experimental results by an average of 5.33%. Therefore, for estimating negative stiffness characteristics of a single ESA unit and different layers of ESA configurations, mathematical modeling is used. These findings validated both the mathematical model and experimental values.

The ESA configuration (UESA or AESA) and the number of layers (1 to 6) were varied. Common trends include:

- **Impact of Current:** Increasing the current increases the electromagnetic force for single-unit ESAs.
- **Effect of Layers:** Adding layers increases force in the force-displacement graph for both UESA and AESA.
- **Negative Stiffness Range:** Additional layers broaden the negative stiffness range.
- **Configuration Comparison:** AESA configurations exhibit higher nonlinearity, greater electromagnetic forces, and greater negative stiffness value compared to UESA for the same current input.

Single ESA Unit Force Characteristics

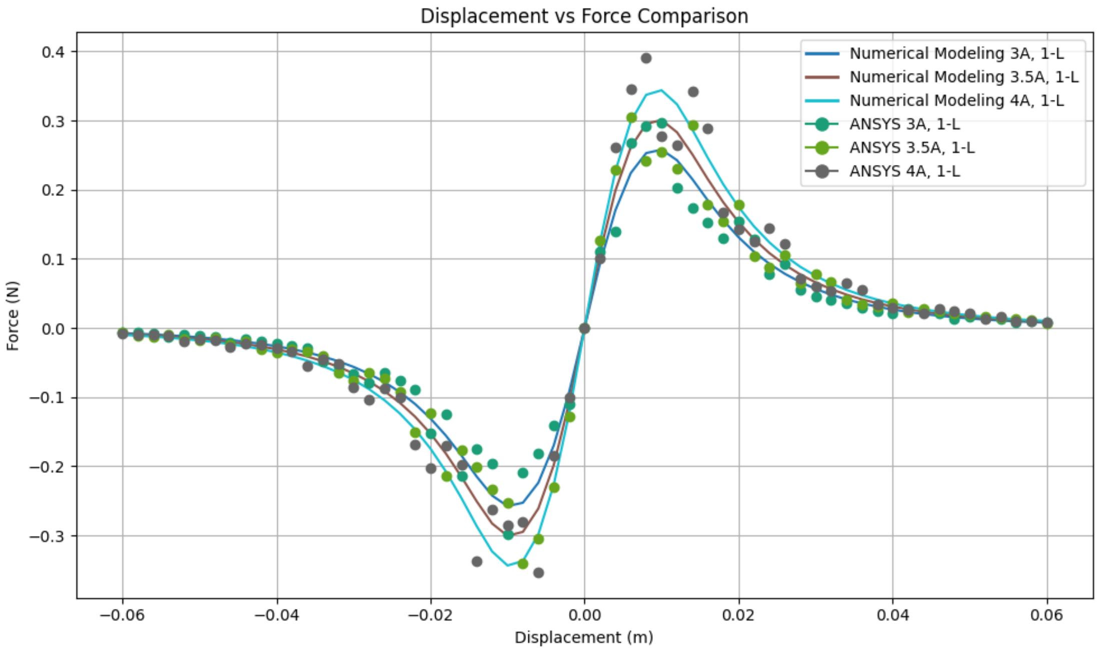

Figure 5.1: Calculated and Simulated Electromagnetic Forces of the ESA unit

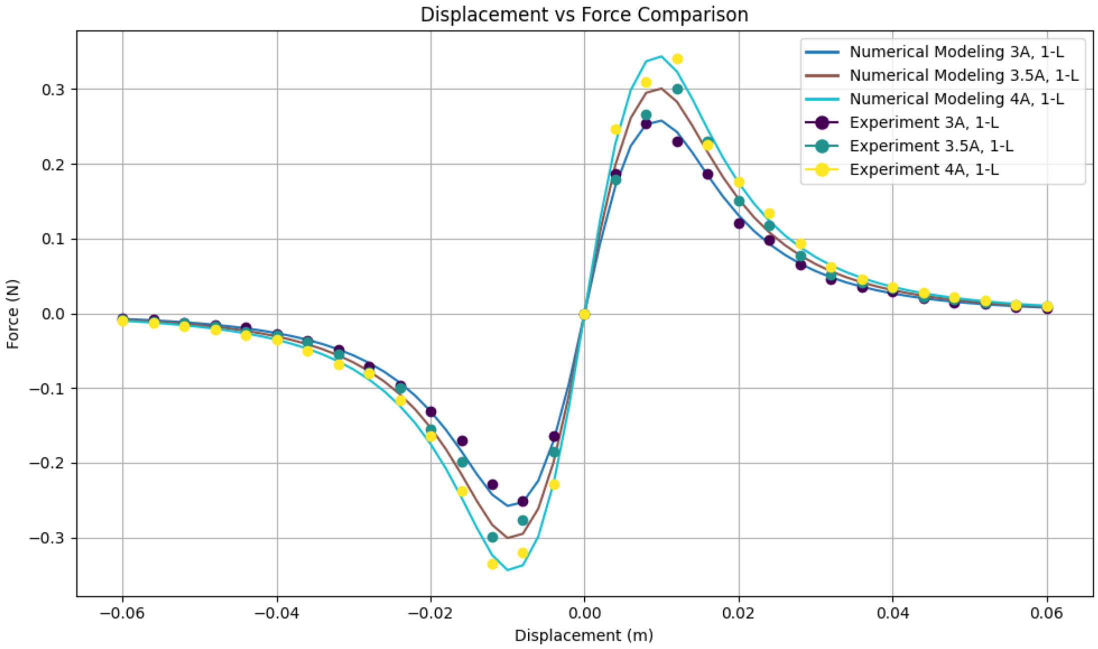

Figure 5.2: Calculated and Measured Electromagnetic Forces of the ESA unit

Fig. 5.1 compares numerical modeling using the filament method in Python with Ansys simulation results for varying control currents in a single ESA unit (1M1C configuration). In this figure, the solid line represents the force between the moving magnet and the static coil calculated by the mathematical model, while the circular markers indicate force measurements from the Ansys simulation. The plot shows only a loose correlation between the forces measured by the two methods, but the overall force trend is consistent.

Similarly, Fig.5.2 compares numerical modeling using the filament method with experimental results for varying control currents in a single ESA unit (1M1C configuration). Here, the solid line represents the force calculated using the mathematical model, and the circular markers indicate force measurements obtained from the load cell. This plot shows a strong correlation between the forces.

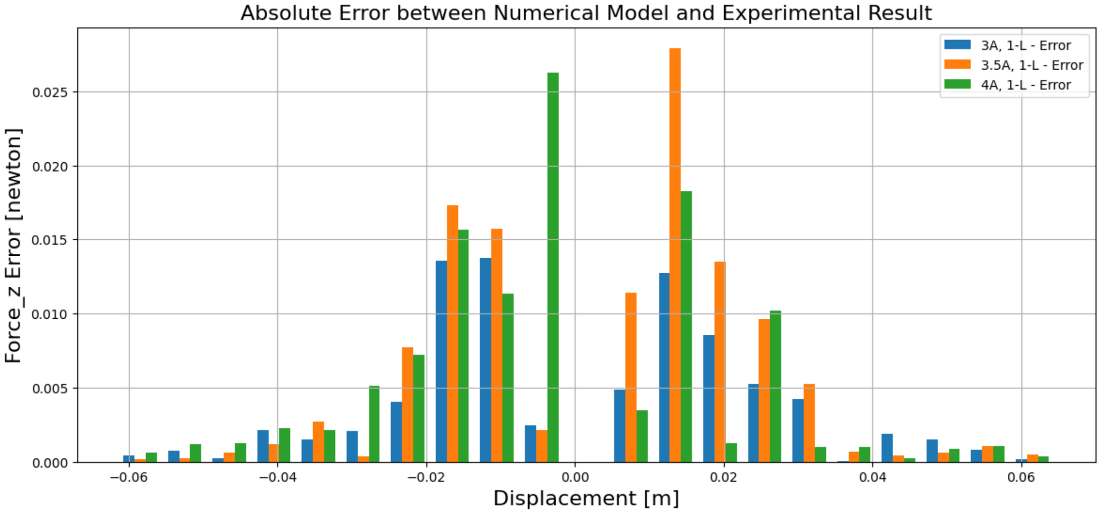

Figure 5.3: Absolute Error between Numerical Model and Experimental Result

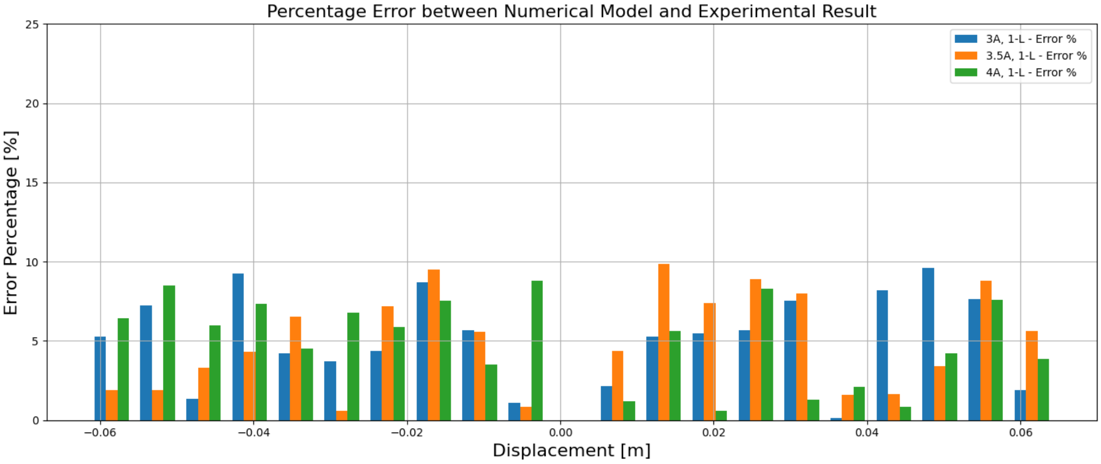

Figure 5.4: Percentage Error between Numerical Model and Experimental Result

Figures 5.3 and 5.4 display the absolute error and error percentage between the force from Eq. (3.5) and experimental data. The maximum error percentage remains below 20%, which is acceptable given experimental imperfections. Importantly, both methods show consistent trends, confirming the analytical model's accuracy.

UESA Configuration Force Characteristics

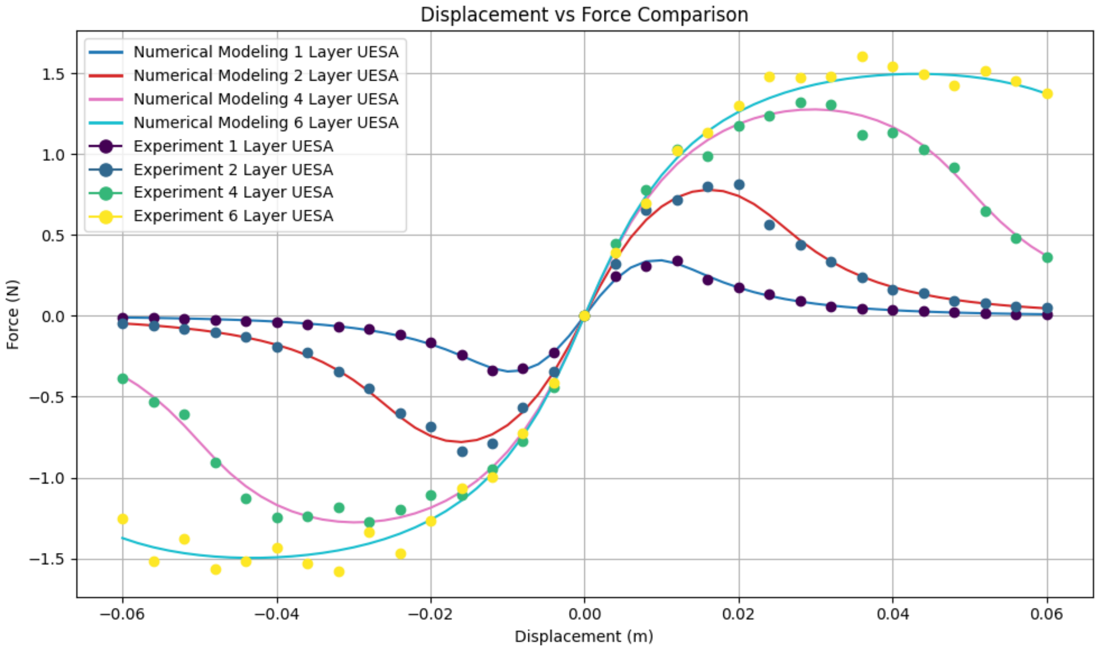

Figure 5.5: Calculated and Measured Electromagnetic Forces of UESA with Different Layers

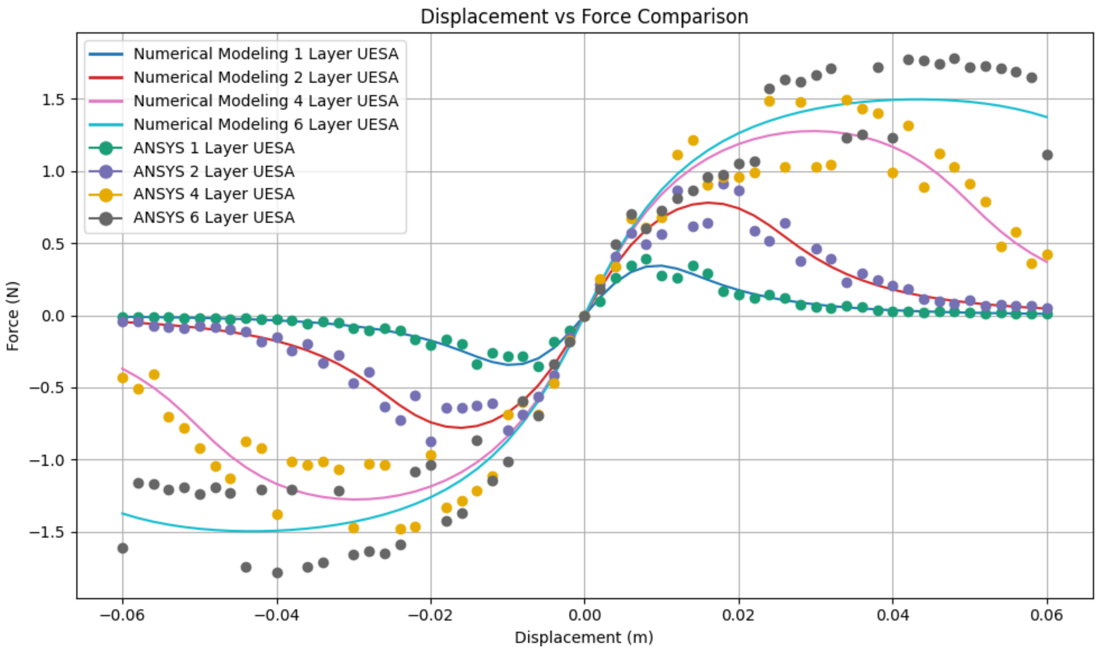

Figure 5.6: Calculated and Simulated Electromagnetic Forces of UESA with Different Layers

Figure 5.5 and 5.6 shows the electromagnetic force between the moving magnet and static coil for different layers of UESA. As layers increase, the electromagnetic force strengthens for the same displacement. Additionally, the peak force (both positive and negative) shifts further from equilibrium.

AESA Configuration Force Characteristics

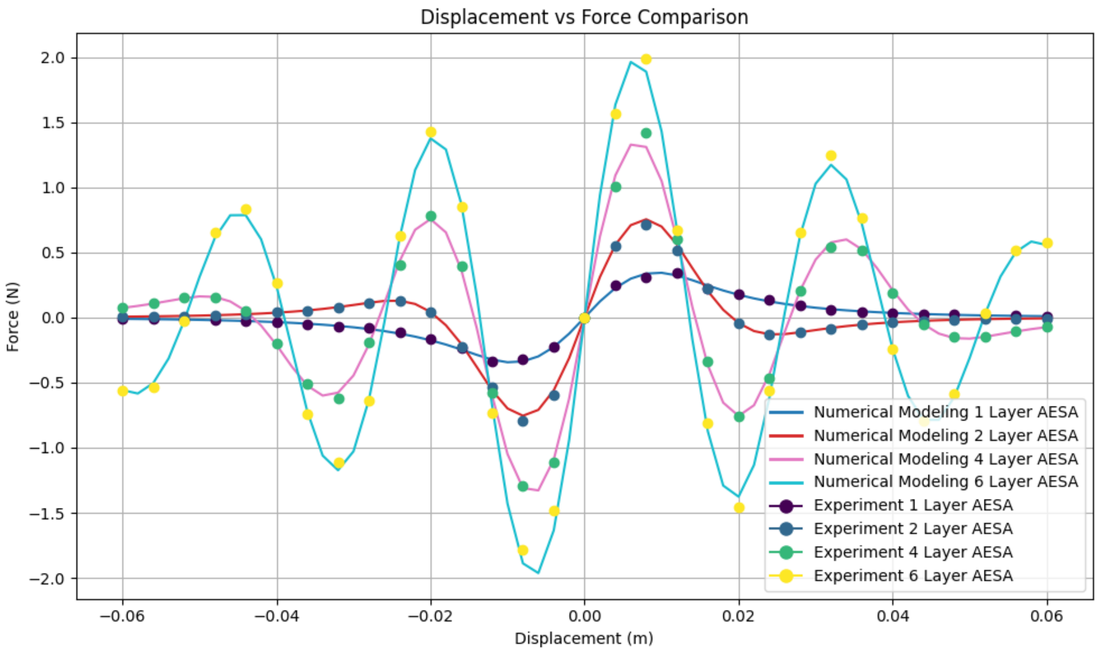

Figure 5.7: Calculated and Measured Electromagnetic forces of AESA with Different Layers

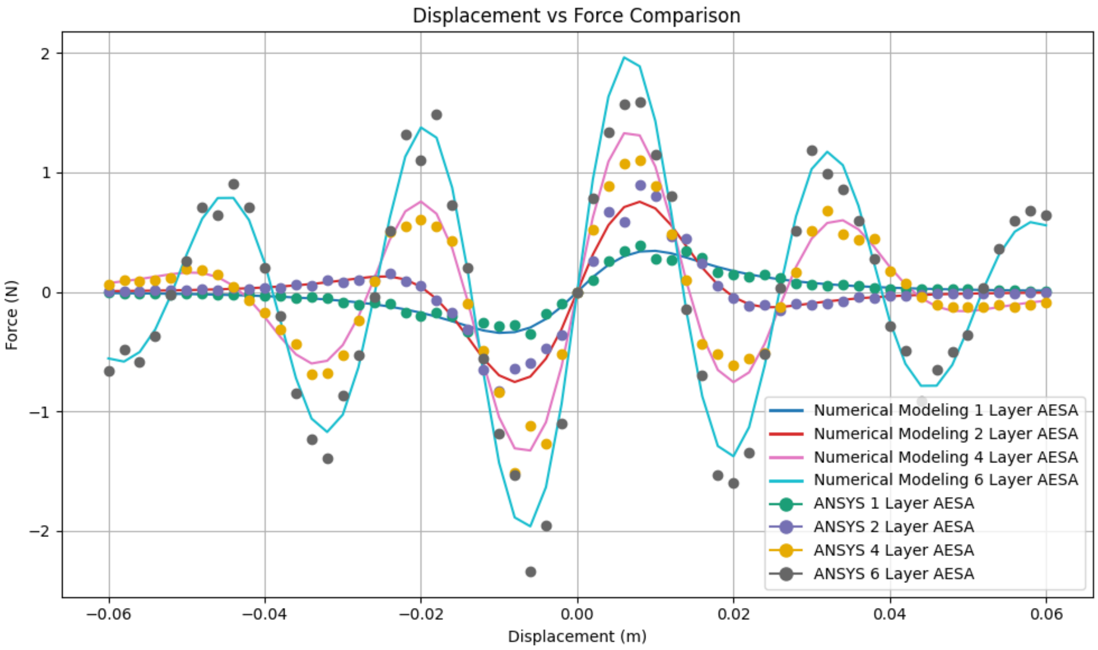

Figure 5.8: Calculated and Simulated Electromagnetic forces of AESA with Different Layers

Figure 5.7 and 5.8 presents the force vs. displacement curve for AESA. The nonlinear behavior is more pronounced in AESA with more layers. Compared to UESA, AESA exhibits higher peak electromagnetic forces. For a constant current, increasing the number of layers raises the electromagnetic force, similar to UESA.

Single ESA Stiffness Characteristics

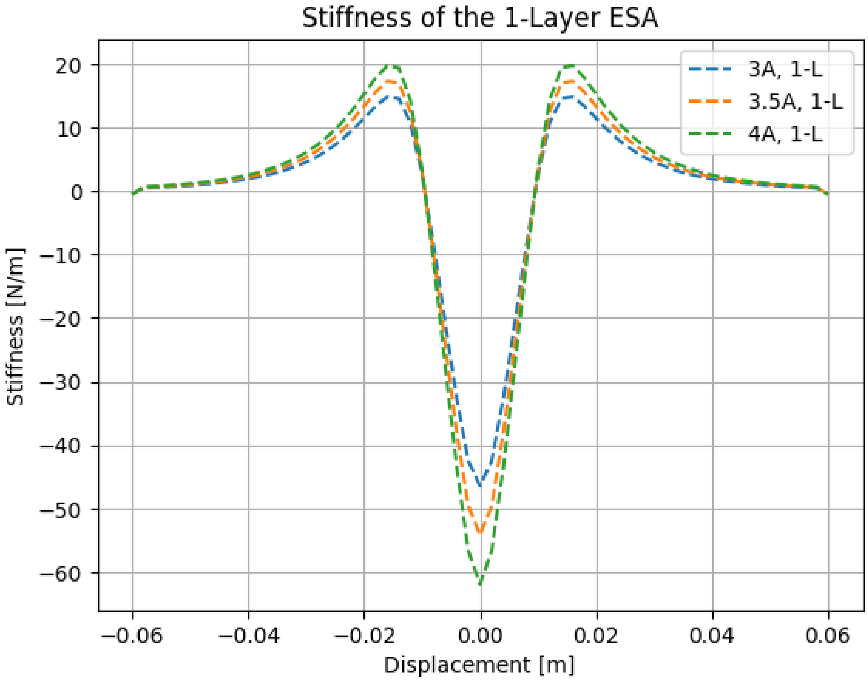

Figure 5.9: Axial Stiffness of the ESA unit under different control currents

Figure 5.9 shows the axial stiffness of a single ESA unit estimated via the mathematical model for various control currents. The stiffness curve near equilibrium is V-shaped. The region where stiffness is negative is termed the negative stiffness region. The displacement at which stiffness becomes zero defines the negative stiffness margin.

When displacement is zero (i.e., the magnet coincides with the coil), negative stiffness reaches its maximum, while electromagnetic force is zero. This ensures that the ESA does not compromise the bearing capacity of the mechanical spring's positive stiffness. As displacement increases, electromagnetic force rises. When stiffness reaches zero, the electromagnetic force peaks (either positive or negative).

If displacement surpasses the negative stiffness threshold, the repulsive force starts decreasing, potentially protecting the isolator from exceeding its operational limits. The rated stiffness is proportional to control current, consistent with Eq. (3.10). The tunable range of negative stiffness is constrained by the maximum coil current (4.0 A in this study). This limit depends on the enameled wire's characteristics. A larger wire diameter allows higher current but reduces the number of turns on the coil.

For coils of the same geometry, the maximum current flowing through the cross-section remains similar regardless of wire diameter. Thus, the stiffness has a limited tunable range. This flexibility allows wire diameter selection based on market availability without restricting the design to a specific size.

UESA Configuration Stiffness Characteristics

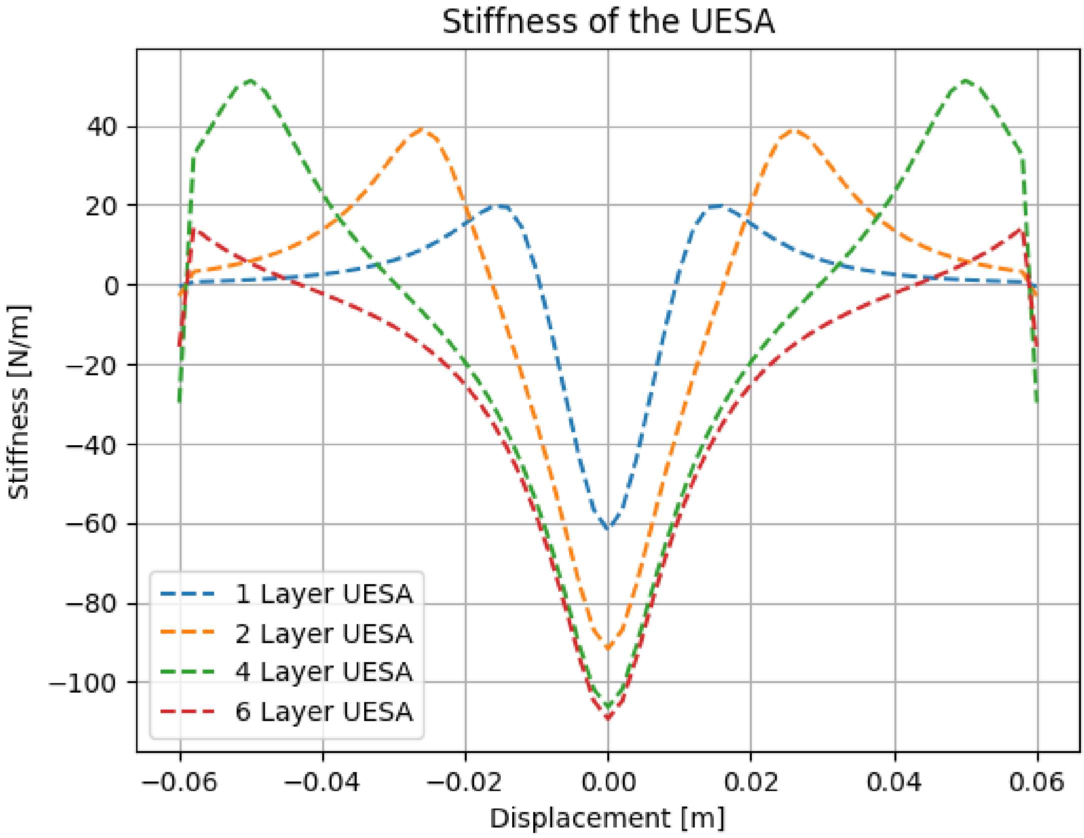

Figure 5.10: Axial Stiffness of UESA with Different Layers

Figure 5.10 presents the stiffness curve for UESA. For a fixed control current of 4 A, increasing UESA layers expands the negative stiffness region but minimally affects the rated negative stiffness. For a 6-layer configuration at 4 A, the maximum negative stiffness is -109.307 N/m.

AESA Configuration Stiffness Characteristics

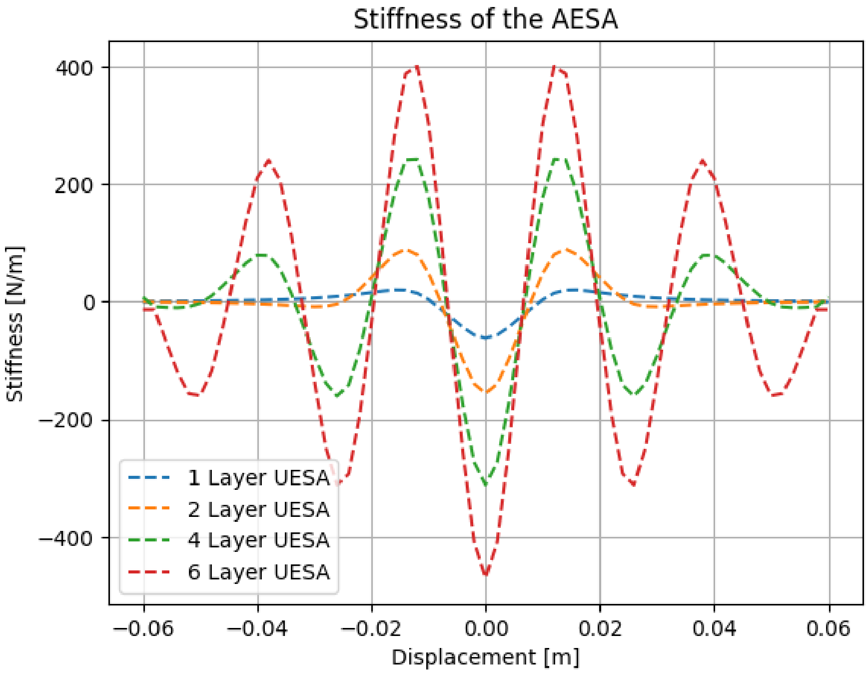

Figure 5.11: Axial Stiffness of AESA with Different Layers

Figure 5.11 illustrates that, unlike UESA, increasing AESA layers results in a linear increase in negative stiffness for a constant current of 4 A. The maximum negative stiffness value, as observed for a 6-layer AESA configuration, was found to be -469.900 N/m. Compared to UESA's axial stiffness, AESA configurations have a narrower displacement range for negative stiffness. Specifically, negative stiffness occurs within a small displacement range of ±7.2 mm from equilibrium.

5.2 Dynamic Modeling of Electromagnetic Force

To simplify force evaluation, the isolator was modeled as a single-degree-of-freedom (SDOF) system, where the force depends on displacement (D) and coil current I_c. Using the curve fitting module in SciPy, parameters f_1 and f_2 were derived. Predicted forces from the dynamic model closely aligned with actual values, achieving satisfactory R^2 values and low Root Mean Square Errors (RMSE).

Dynamic Modeling

The conceptualized vibration isolator is a typical single-degree-of-freedom (S-DOF) system with only permissible vertical motion. Fig. 5.12 shows the equivalent dynamic model of the vibration isolator.Table:5.1 lists the physical parameters of the isolator.

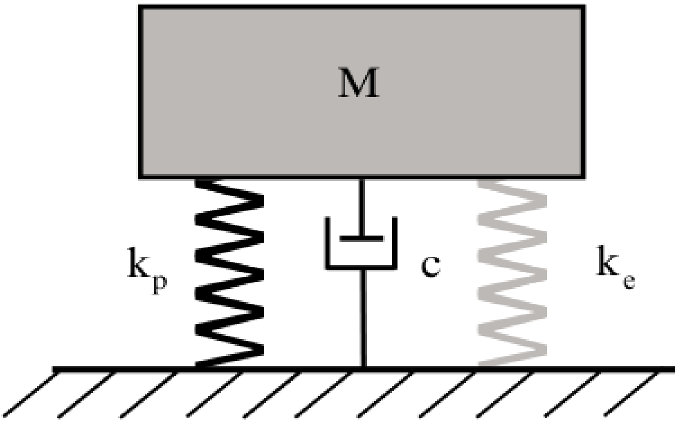

Figure 5.12: Equivalent Model of SDOF Vibration Isolation System

Table 5.1: Physical parameters of isolator

Parameter	**m**	k_p	k_n	ω_p	ω_{pn}
Unit	kg	N/m	N/m	rad/s	rad/s
Value	1.4	2270	-469.900	6.4087	5.7070

Table 5.2: Physical parameters of shake table

Parameter	**m**	k_p	ω
Unit	kg	N/m	rad/s
Value	20	4 x 5560	5.30

The integral expression of the electromagnetic force given by Eq. (2.8) is too complex to establish the dynamic equation of the isolator. Therefore, to simplify the dynamic equation of the isolator, a simplified expression for the electromagnetic force is needed. By examining the curve form in Fig. 5.13 the electromagnetic force can be approximated by a cubic polynomial function with respect to displacement D. Since the electromagnetic force is also proportional to the current passing through the coil, the final cubic polynomial function to approximate the force takes the following form:

$$F_e(D, I_c) = f_1 I_c D + f_2 I_c D^3 \qquad [19] \tag{5.1}$$

The dynamic equation of the isolator can be expressed as follows:

$$m\ddot{D} + c\dot{D} + k_p D - f_1 I_c D - f_2 I_c D^3 = 0 \qquad [17] \tag{5.2}$$

Let x_0 represent the displacement of the base excitation and x_1 denote the displacement of the mass. The relative displacement of the mass with respect to the base is y, where $y = D$. The base excitation is described by $x_0 = X_0 \cos(\omega t + \theta)$ The dynamic equation governing the isolator is given as:

$$m\ddot{D} + c\dot{D} + \left(k_p - f_1 I_c - f_2 I_c D^2\right) D = -m\ddot{x}_0 \qquad [17] \tag{5.3}$$

and the proceeding equation can be nondimensionalized as:

$$\ddot{x} + 2\zeta\dot{x} + x + \delta x_0^2 x^3 = \Omega^2 \cos\Omega\tau \tag{5.4}$$

where $x = \frac{D}{x_0}$, $\omega_n = \sqrt{\frac{k_p - f_1 I_c}{m}}$, $\zeta = \frac{c}{2m\omega_n}$, $\delta = \frac{f_2 I_c}{k_p - f_1 I_c}$, $\Omega = \frac{\omega}{\omega_n}$, $\tau = \omega_n t$.

Equation (5.4) represents a Duffing equation with a harmonic excitation term, which can be solved using the harmonic balance method (HBM). The assumed solution is given by $x = X\cos(\Omega\tau + \theta)$, where θ denotes the phase difference between the excitation and the response. Thus, Choosing an appropriate value of θ, the solution of Eq. (5.4) can be expressed as:

$$x = X\cos(\beta\tau) \qquad [17] \tag{5.5}$$

Substituting this into Eq. (22), we obtain the following system of equations:

$$\begin{cases} (\beta^2 X + X + \frac{3}{4}\delta X^3) = \beta^2\cos\theta, \\ -2\beta\xi X = \beta^2 \sin\theta. \end{cases} \qquad [17] \tag{5.6}$$

Solving Eq. (5.6), the relationship between β and X is given by:

$$\beta^2 = \frac{X^2(4 + 3\delta X^2) - 8\xi X^2 \pm \sqrt{(8\xi^2 X^2 - 4X^2 - 36\delta X^4)^2 - (X^2 - 1)(4X + 36\delta X^3)^2}}{4(X^2 - 1)} \qquad [17] \tag{5.7}$$

The absolute displacement of the mass is:

$$x_1 = xX_0 + X_0\cos(\beta\tau) = (X + 1)X_0\cos(\beta\tau) - \xi X\sin(\beta\tau) \qquad [17] \tag{5.8}$$

Thus, the transmissibility from the base to the mass is:

$$T = \left|\frac{X_1}{X_0}\right| = \sqrt{1 + X^2 + 2X\cos\theta} \qquad [17] \tag{5.9}$$

The term $\cos\theta$ can be obtained from Eq. (5.6). Substituting this value into Eq. (5.9), the transmissibility is rewritten as:

$$T = \sqrt{1 + X^2 + \frac{2X}{\beta^2}\left(\beta^2 X + X + \frac{3}{4}\delta X^3\right)} \qquad [17] \tag{5.10}$$

Thus, the transmissibility of the nonlinear dynamic system described in Eq. (5.4) can be determined using Eqs. (5.6) and (5.10). If the coefficient δ is sufficiently small, the isolator exhibits weak nonlinearity, allowing the dynamic equation (5.3) to be approximated as linear. In this case, the displacement transmissibility from the base to the mass is given by:

$$T = \sqrt{\frac{(k_p - f_1 I_c)^2 + (c\omega)^2}{(k_p - f_1 I_c - m\omega^2)^2 + (c\omega)^2}} \qquad [17] \tag{5.11}$$

The natural frequency of the system is then expressed as:

$$f_n = \frac{1}{2\pi}\sqrt{\frac{k_p - f_1 I_c}{m}} \qquad [17] \tag{5.12}$$

5.2.1 Curve Fitting

For the simplified expression of the electromagnetic force, we require the values of f_1 and f_2. To calculate these values, we utilize the `curve_fit` function from the `scipy` library:

```
from scipy.optimize import curve_fit
```

First, we defined a function that returns the required polynomial function:

```
def dynamic_func(D, f1, f2):
    return (f1 * D + f2 * D^3)
```

Next, we passed this `dynamic_func` along with the force and displacement values obtained from the mathematical model to the `curve_fit` function. The function returns the f_1 and f_2 parameters:

```
params, covariance = curve_fit(dynamic_func, disp, force, p0
   =[1, 1])
```

Using the f_1 and f_2, we then predict the force with the `dynamic_func`:

```
predicted_force = dynamic_func(disp, f_1, f_2)
```

The predicted force value is then compared with the original force from the mathematical model to calculate the R^2 and RMSE. The table below shows the f_1, f_2, R^2, and RMSE values for the 2, 4, and 6-layer AESA and UESA configurations.

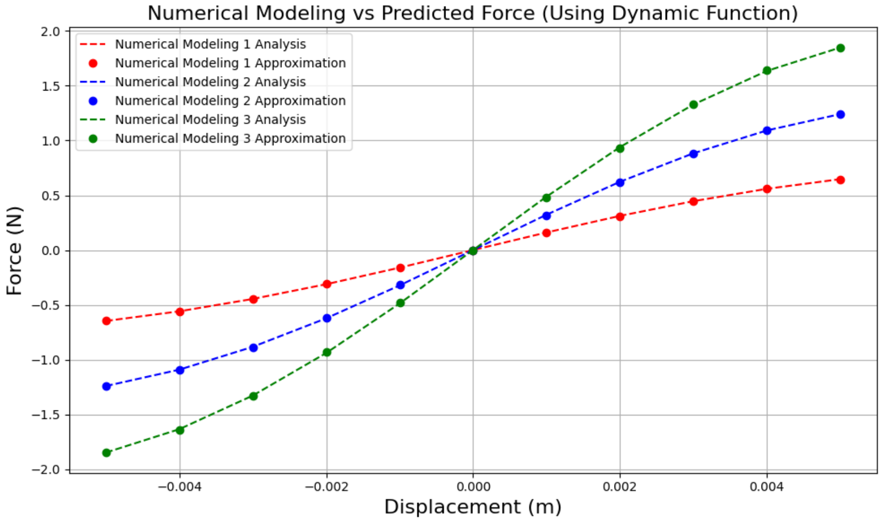

Figure 5.13: Approximated Force for the AESA Configurations.

Table 5.3: Values of f_1, f_2, R^2, and RMSE for AESA configurations.

Configuration	f_1 (N m^{-1} A^{-1})	f_2 (N m^{-3} A^{-1})	R^2	RMSE (N)
2-Layer	160.093541	-1.234785e+06	0.999988	0.001520
4-Layer	321.565205	-2.954001e+06	0.999983	0.003561
6-Layer	485.623115	-4.668758e+06	0.999981	0.005603

Figure 5.13 shows the approximated force and the analyzed force. The approximated force closely fits the analyzed force, and the R^2 values are greater than 0.9999 for all the curves. For the 6-layer AESA, the predicted force does not fit with the original analyzed force curve (see Table:5.3), and the RMSE is higher than for the other configurations, indicating the need for a better algorithm to achieve better results.

5.2.2 Vibration Isolator Performance

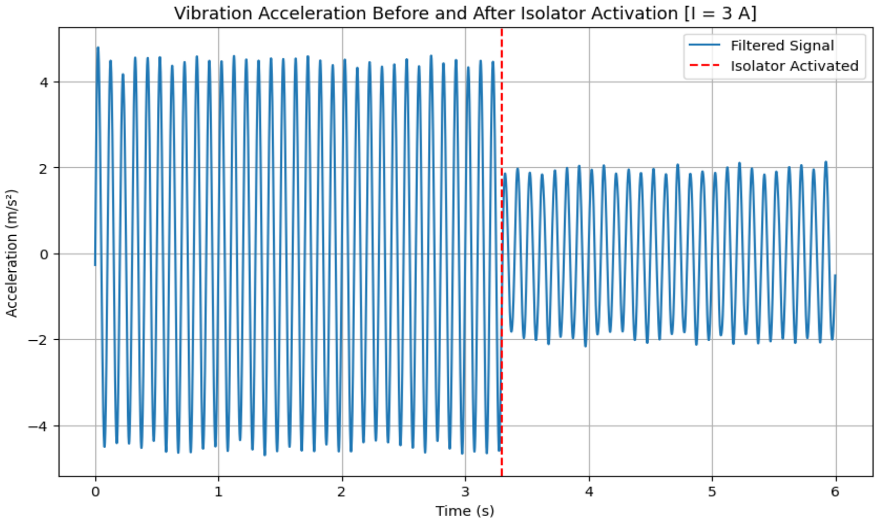

Figure 5.14: Time-response of the isolator with control current of 3A

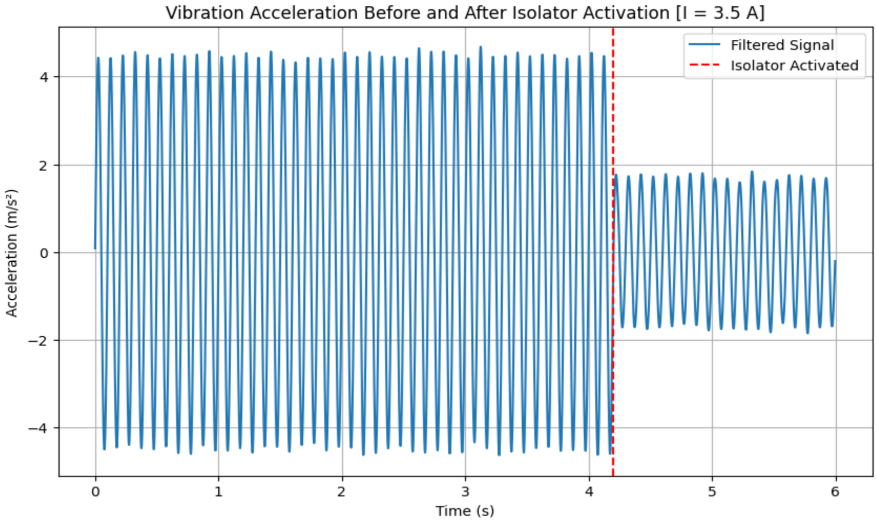

Figure 5.15: Time-response of the isolator with control current of 3.5A

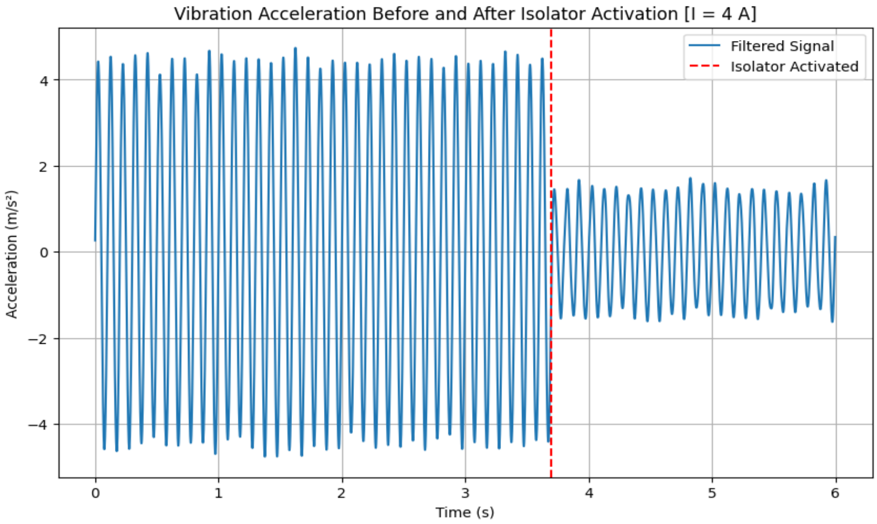

Figure 5.16: Time-response of the isolator with control current of 4A

Clearly,as shown in 5.14 - 5.16, increasing the current supplied to the electromagnet improved the vibration isolation performance of the isolator, as shown by the decrease in the RMS value of acceleration when the current was increased from 3 A to 3.5 A and 4 A. The baseline acceleration at 0 A was 4.5 m/s^2, and it decreased to 2 m/s^2, 1.73 m/s^2, and 1.48 m/s^2 for the respective current values.

Moreover, the results demonstrate the tunability of this electromagnetic isolator: by adjusting the current, one can tailor the vibration isolation performance for different operational conditions. However, it is important to note the potential trade-off between improved isolation and higher power consumption. In practice, an optimal current level might balance effective isolation with acceptable energy usage. Future work could investigate more advanced control algorithms or coil configurations to optimize both performance and power requirements.

5.3 Limitations

- **Single Charge Amplifier:** With only one charge amplifier available, we couldn't record both the excitation signal and the isolated load's vibration simultaneously, preventing direct transmissibility measurement.
- **Plywood Shake Table:** Due to the lack of a properly sized aluminum block, plywood was used for the prototype. While cost-effective and flexible, this may affect performance.
- **Weak Magnets:** The N35 magnets used have a strength of 0.345 T. This limits negative stiffness and reduces isolation performance.
- **Time Constraints:** Advanced optimization, such as coil current tuning for AESA/UESA configurations, remains incomplete and will be addressed in later phases.

5.4 Problems Faced

- Instrumentation and subsystem integration issues, particularly sensor calibration and data analysis.
- Limited procurement options, forcing reliance on high-volume suppliers, causing potential delays and wastage.
- Inexperience in advanced theoretical and mathematical modeling limits formulation accuracy.
- Delays in prototyping due to iterative manufacturing

5.5 Budget Analysis

Table 5.4: RESOURCES AND BUDGET MANAGEMENT

S.No	**Item**	**Qty.**	**Estimated Cost (NPR)**	**Remarks**	**Source**
1	Neodymium Magnet (N35)	6	10000	Bought	India (Patel Magnetic)
2	Mechanical spring	2 Doz.	25000	Bought	USA(Lee Spring/McMaster-Carr)
3	PLA filament (1.75mm)	1	2600	Sponsored	DMAE
4	Copper coil (16 SWG)	10kg	20000	Sponsored	Nepal (Litmus Cables)
5	Voltage regulator (step down)	1	160	Sponsored	DMAE
6	Linear Bearing	12	14075	Bought	Nepal
7	Stainless Steel (8mm)	12ft	800	Bought	Nepal
8	Miscellaneous Expenses	—	5000	Bought	Nepal
Total			**77,635**		

5.6 Work Schedule (Gantt Chart)

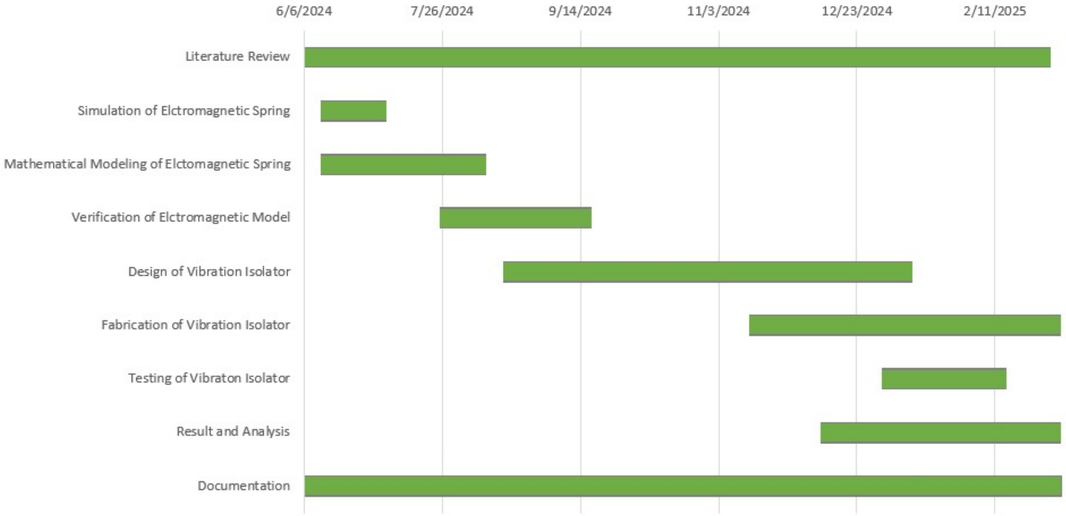

Figure 5.17: Gantt Chart Depicting the Workflow and Timeline

CHAPTER 6

CONCLUSION AND FUTURE ENHANCEMENT

6.1 Conclusion

The project has established a strong foundation for and demonstrated a working model of an electromagnetic spring based vibration isolator. Key achievements include implementing a Python-based mathematical model to quantify electromagnetic force (1.98 N) and stiffness (-469.900 N/m) for Six-layer AESA configurations, and verifying these models through ANSYS simulations and experimental data. The results highlight the feasibility of tuning negative stiffness ranges with the supplied current coil and thus optimizing force-displacement behavior. Designs for the isolator body and shake table have been successfully completed with cost effective 3D printing filaments and plywood respectively for the time being, making room for future revisions and enhancements. Regardless, current results and demonstrations ensure alignment with both theoretical and practical objectives.

6.2 Scope for Future Enhancement

Future work can focus on extensive testing of force and stiffness characteristics for additional ESA configurations beyond UESA and AESA. Efforts can also be directed toward exploring alternative materials and manufacturing techniques to improve the isolator body and shake table. Expanding the isolator's application to industrial and laboratory settings is another key area, with the potential to develop a vibration isolation table based on the current mechanisms. Additionally, implementing control systems will enable semi-active operation, allowing the system to self-regulate. The ultimate goal is to develop a closed-loop vibration isolation system that dynamically adjusts the supplied current, and in turn the negative stiffness, based on payload mass and input vibration frequency.

BIBLIOGRAPHY

[1] Z. Ma, R. Zhou, and Q. Yang, “Recent Advances in Quasi-Zero Stiffness Vibration Isolation Systems: An Overview and Future Possibilities,” *Machines*, vol. 10, p. 813, sep 16 2022. [Online; accessed 2024-06-11].

[2] A. Carrella, M. Brennan, and T. Waters, “Static analysis of a passive vibration isolator with quasi-zero-stiffness characteristic,” *Journal of Sound and Vibration*, vol. 301, pp. 678–689, 4 2007. [Online; accessed 2024-06-10].

[3] A. Shiri and A. Shoulaie, “A new methodology for magnetic force calculations between planar spiral coils,” *Progress In Electromagnetics Research*, vol. 95, pp. 39–57, 2009.

[4] S. Sun, J. Yang, W. Li, H. Deng, H. Du, and G. Alici, “Development of a novel variable stiffness and damping magnetorheological fluid damper,” *Smart Materials and Structures*, vol. 24, p. 085021, jul 15 2015. [Online; accessed 2024-06-10].

[5] J.-D. Wu, W.-K. Tseng, and R.-J. Chen, “A study of an electrorheological fluid-based mount for broadband vibration isolation in a squeeze mode,” *Proceedings of the Institution of Mechanical Engineers, Part D: Journal of Automobile Engineering*, vol. 220, pp. 313–320, mar 1 2006. [Online; accessed 2024-06-10].

[6] A. Carrella, M. Brennan, I. Kovacic, and T. Waters, “On the force transmissibility of a vibration isolator with quasi-zero-stiffness,” *Journal of Sound and Vibration*, vol. 322, pp. 707–717, 5 2009. [Online; accessed 2024-06-10].

[7] A. Carrella, M. Brennan, T. Waters, and V. Lopes, Jr., “Force and displacement transmissibility of a nonlinear isolator with high-static-low-dynamic-stiffness,” *International Journal of Mechanical Sciences*, vol. 55, pp. 22–29, 2 2012. [Online; accessed 2024-06-10].

[8] I. Kovacic, M. J. Brennan, and T. P. Waters, “A study of a nonlinear vibration isolator with a quasi-zero stiffness characteristic,” *Journal of Sound and Vibration*, vol. 315, pp. 700–711, 8 2008. [Online; accessed 2024-06-10].

[9] X. Huang, X. Liu, J. Sun, Z. Zhang, and H. Hua, “Vibration isolation characteristics of a nonlinear isolator using Euler buckled beam as negative stiffness corrector: A theoretical and experimental study,” *Journal of Sound and Vibration*, vol. 333, pp. 1132–1148, 2 2014. [Online; accessed 2024-06-11].

[10] Z. Wu, X. Jing, J. Bian, F. Li, and R. Allen, “Vibration isolation by exploring bio-inspired structural nonlinearity,” *Bioinspiration & biomimetics*, vol. 10, no. 5, p. 056015, 2015.

[11] X. Sun, J. Xu, F. Wang, and S. Zhang, “A novel isolation structure with flexible joints for impact and ultralow-frequency excitations,” *International Journal of Mechanical Sciences*, vol. 146, pp. 366–376, 2018.

[12] A. G. Izard, R. F. Alfonso, G. McKnight, and L. Valdevit, “Optimal design of a cellular material encompassing negative stiffness elements for unique combinations of stiffness and elastic hysteresis,” *Materials & Design*, vol. 135, pp. 37–50, 2017.

[13] H. Fan, L. Yang, Y. Tian, and Z. Wang, “Design of metastructures with quasi-zero dynamic stiffness for vibration isolation,” *Composite Structures*, vol. 243, p. 112244, 2020.

[14] A. Carrella, M. Brennan, T. Waters, and K. Shin, “On the design of a high-static–low-dynamic stiffness isolator using linear mechanical springs and magnets,” *Journal of Sound and Vibration*, vol. 315, pp. 712–720, 8 2008. [Online; accessed 2024-06-10].

[15] N. Zhou and K. Liu, “A tunable high-static–low-dynamic stiffness vibration isolator,” *Journal of Sound and Vibration*, vol. 329, pp. 1254–1273, 4 2010. [Online; accessed 2024-06-10].

[16] Y. Zheng, X. Zhang, Y. Luo, B. Yan, and C. Ma, “Design and experiment of a high-static–low-dynamic stiffness isolator using a negative stiffness magnetic spring,” *Journal of Sound and Vibration*, vol. 360, pp. 31–52, 1 2016. [Online; accessed 2024-06-10].

[17] S. Yuan, Y. Sun, J. Zhao, K. Meng, M. Wang, H. Pu, Y. Peng, J. Luo, and S. Xie, “A tunable quasi-zero stiffness isolator based on a linear electromagnetic spring,” *Journal of Sound and Vibration*, vol. 482, p. 115449, 2020.

[18] Y. Sun, J. Zhao, M. Wang, Y. Sun, H. Pu, J. Luo, Y. Peng, S. Xie, and Y. Yang, “High-static–low-dynamic stiffness isolator with tunable electromagnetic mechanism,” vol. 25, no. 1, pp. 316–326.

[19] H. Pu, S. Yuan, Y. Peng, K. Meng, J. Zhao, R. Xie, Y. Huang, Y. Sun, Y. Yang, S. Xie, J. Luo, and X. Chen, “Multi-layer electromagnetic spring with tunable negative stiffness for semi-active vibration isolation,” *Mechanical Systems and Signal Processing*, vol. 121, pp. 942–960, 2019.

[20] W. Robertson, B. Cazzolato, and A. Zander, “A simplified force equation for coaxial cylindrical magnets and thin coils,” *IEEE Transactions on magnetics*, vol. 47, no. 8, pp. 2045–2049, 2011.

[21] H. Pu, S. Yuan, Y. Peng, K. Meng, J. Zhao, R. Xie, Y. Huang, Y. Sun, Y. Yang, S. Xie, J. Luo, and X. Chen, “Multi-layer electromagnetic spring with tunable negative stiffness for semi-active vibration isolation,” *Mechanical Systems and Signal Processing*, vol. 121, pp. 942–960, 4 2019. [Online; accessed 2024-06-10].

APPENDIX: PYTHON IMPLEMENTATION OF FILAMENT METHOD

```
def segment_current(turns, total_current, nr, na):
    """
    Calculate the current for each segment based on the total current and number of segments.
    total_current: Total current passing through the coil
    nr: Number of radial segments
    na: Number of axial segments
    """
    curr = (total_current * turns) / (nr * na)
    return curr

def force_between_segments(i1, i2, r_k, r_j, z_il):
    """
    Calculate the force between two segments using elliptic integrals.
    """
    k_prime_val = k_prime(r_k, r_j, z_il)
    prefactor = (MU_0 * i1 * i2 * z_il * k_prime_val) / (2 * np.sqrt(r_k * r_j) * (1 - k_prime_val**2))

    # Elliptic integrals of the first (K) and second (E) kind
    K_k = ellipk(k_prime_val**2)
    E_k = ellipe(k_prime_val**2)

    force =  prefactor * ((1 - k_prime_val**2) * K_k - (1 - (k_prime_val**2 / 2)) * E_k)

    return force

def force_MES(sequence, turn_coil, turn_mag, i_coil, i_mag, v, u, w, r_coil_i, r_coil_o, r_mag_i, r_mag_o, h, range_l, range_h, step):
    """
    Calculate the total magnetic force between two coils and a magnet at different distances.
Parameters:
    sequence (int): A parameter that defines the coil and magnet arrangement.
    turn_coil (int): The number of turns in the coil.
    turn_mag (int): The number of turns in the magnet.
    i_coil (float): The current in the coil (in amperes).
    i_mag (float): The current in the magnet (in amperes).
    v (float): The voltage applied to the system.
    u (float): Permeability constant.
    w (float): A parameter that might define geometry or other constants.
    r_coil_i (float): The inner radius of the coil.
```

```
r_coil_o (float): The outer radius of the coil.
r_mag_i (float): The inner radius of the magnet.
r_mag_o (float): The outer radius of the magnet.
h (float): A constant related to height or other geometry
   of the system.
range_l (int): The lower limit of the distance range (in
   millimeters).
range_h (int): The upper limit of the distance range (in
   millimeters).
step (int): The step size for iterating over the distance
   range.
Returns:
list: A list of tuples, where each tuple contains the
   distance (in meters) and the corresponding total
   magnetic force (in Newtons) at that distance.
"""
output = []
for i in range(-range_l, range_h, step):
    z_distance = i / 1000  # Convert distance to meters
    total_force_1 = total_force_S_MLE(sequence, turn_coil,
       turn_mag, -i_coil, i_mag, v, 1, u, w, r_coil_i,
       r_coil_o, r_mag_o, r_mag_o, z_distance, h, h)

    total_force_2 = total_force_S_MLE(sequence, turn_coil,
       turn_mag, -i_coil, -i_mag, v, 1, u, w, r_coil_i,
       r_coil_o, r_mag_i, r_mag_i, z_distance, h, h)
    total_force = total_force_1 + total_force_2

    print(f"Total␣Magnetic␣Force␣between␣Coils␣{z_distance
       }:␣{total_force:.4e}␣N")
    output.append((z_distance, total_force))

return output
```

APPENDIX: DRAWING

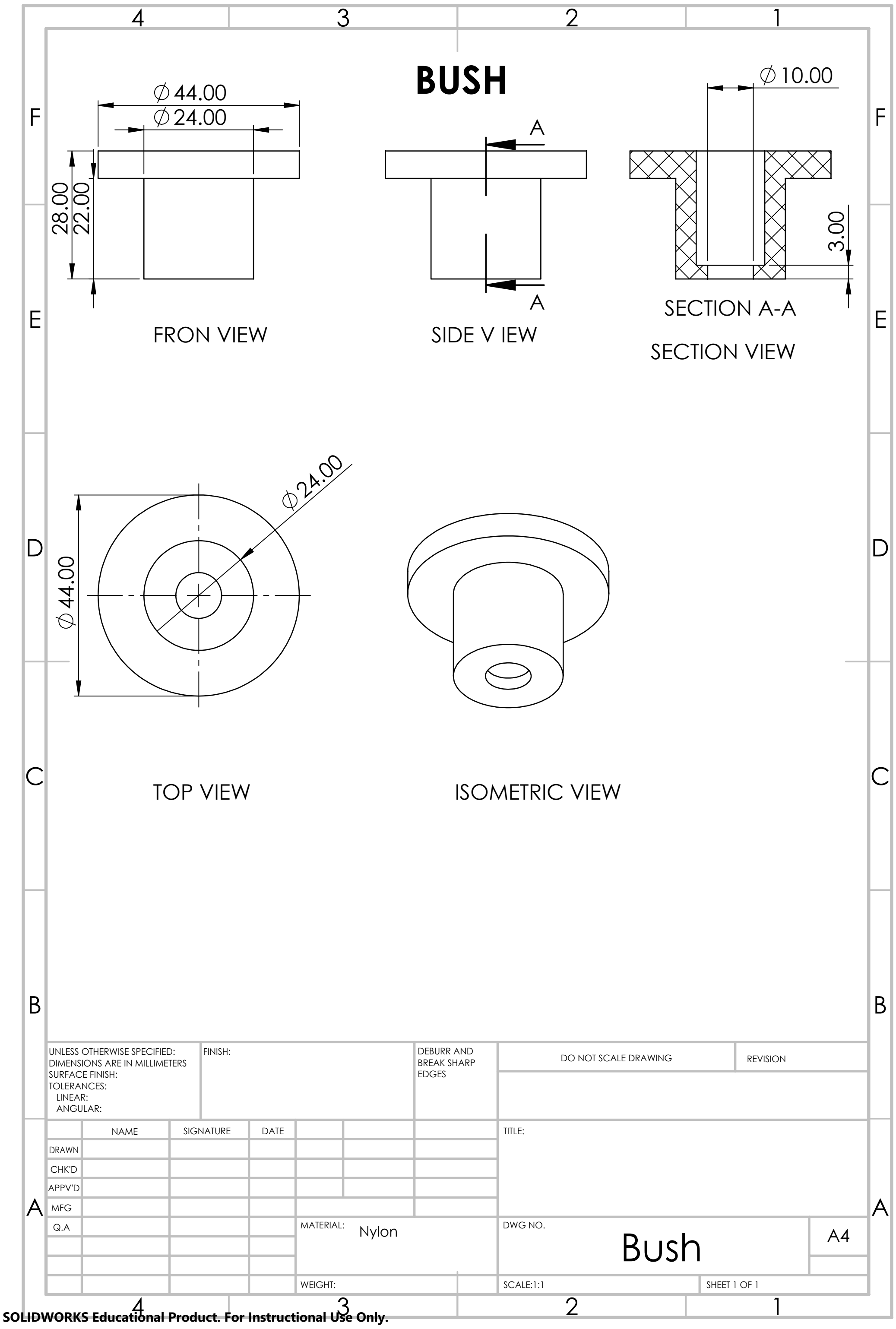

Figure 6.1: Engineering Drawing of Isolator Body

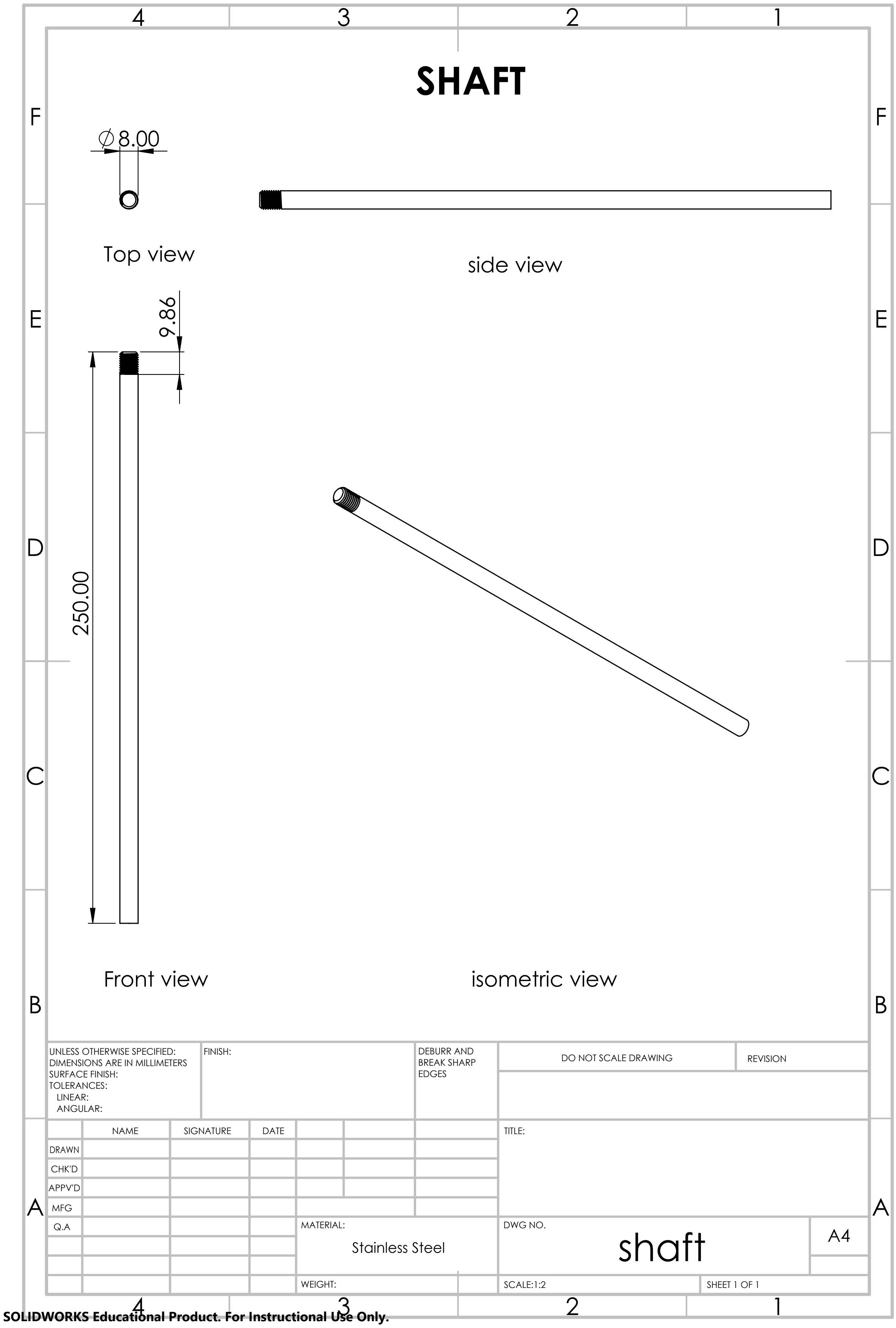

Figure 6.2: Engineering Drawing of Shaft

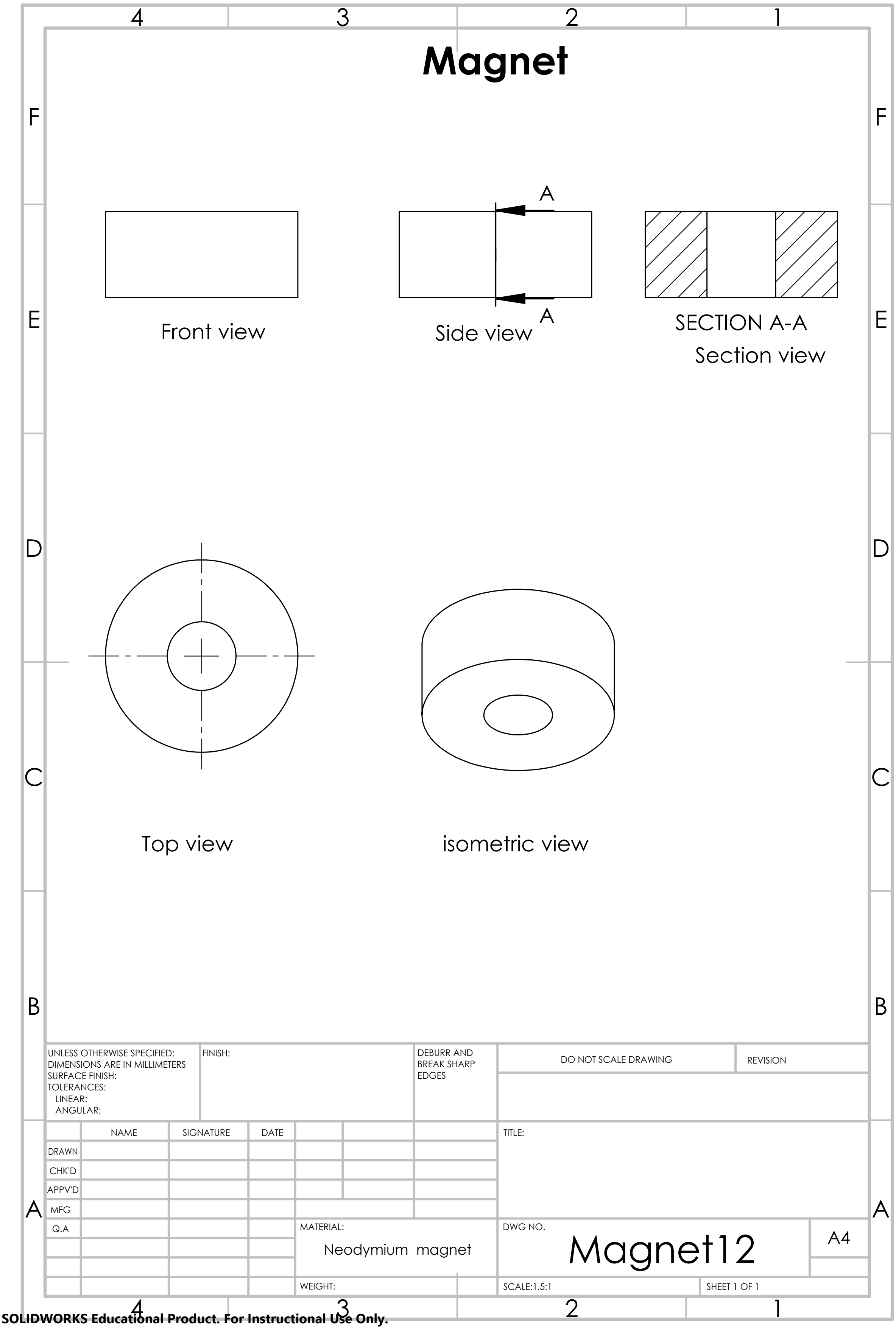

Figure 6.3: Engineering Drawing of Magnet Assembly

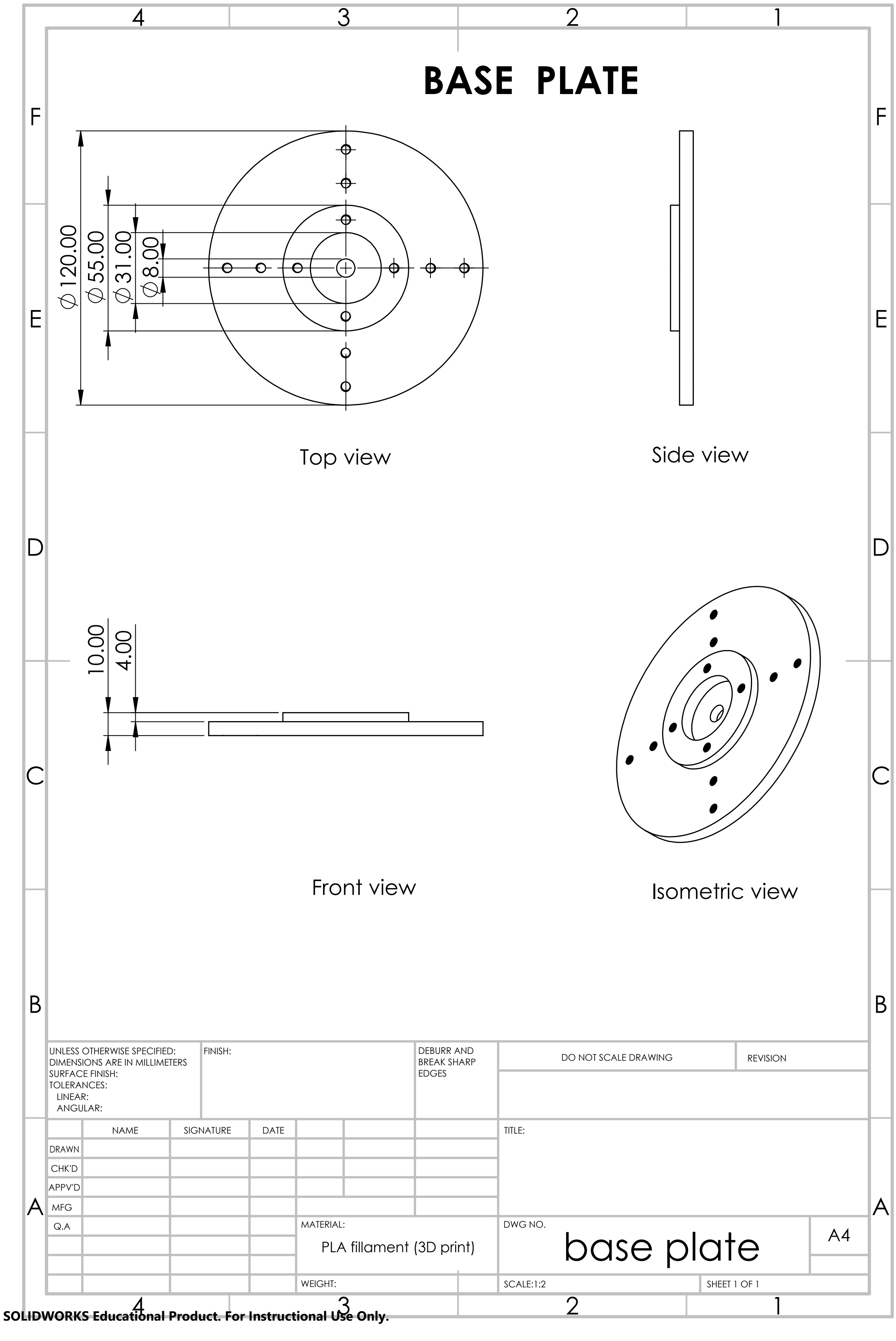

Figure 6.4: Engineering Drawing of Base Plate

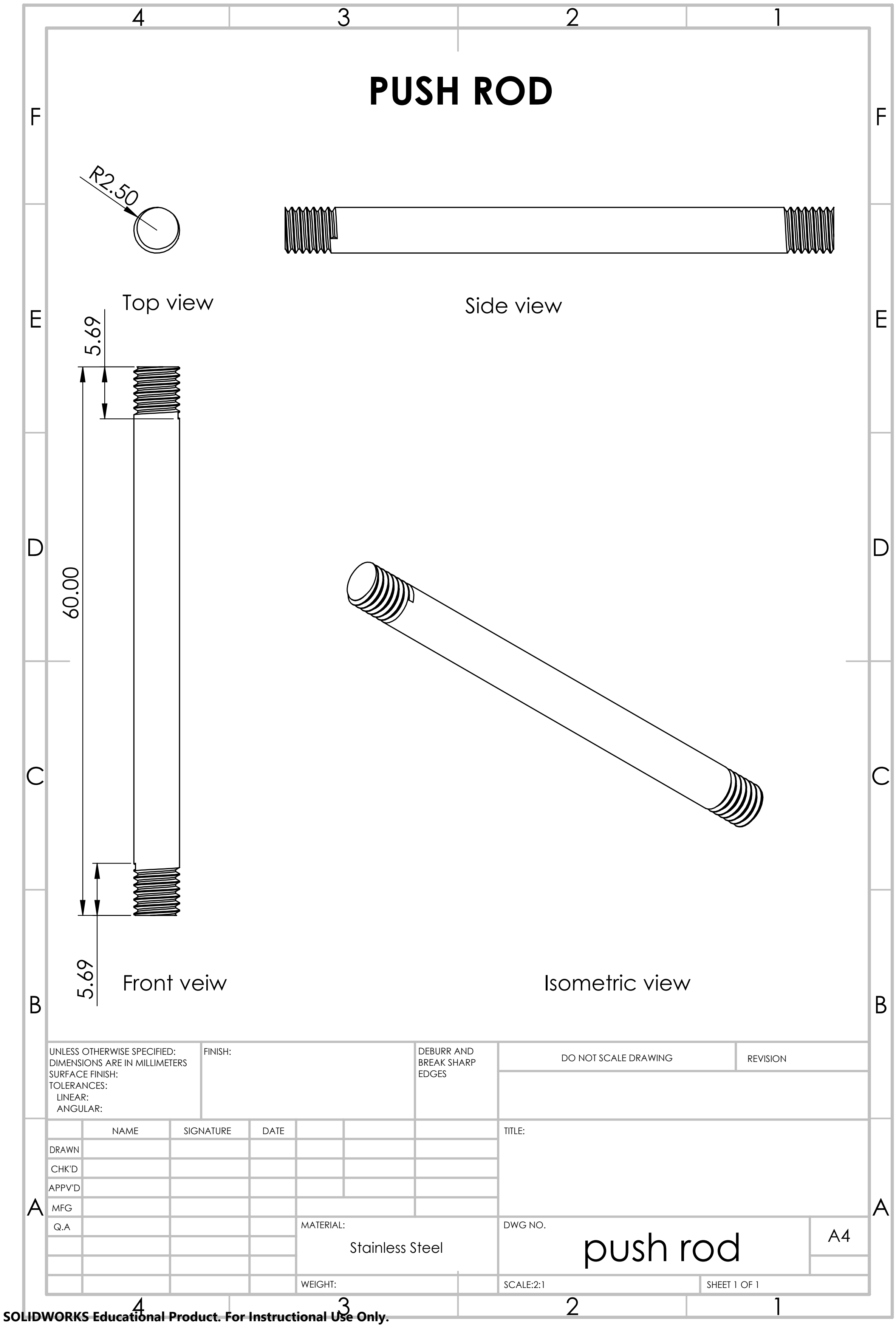

Figure 6.5: Engineering Drawing of Push Rod

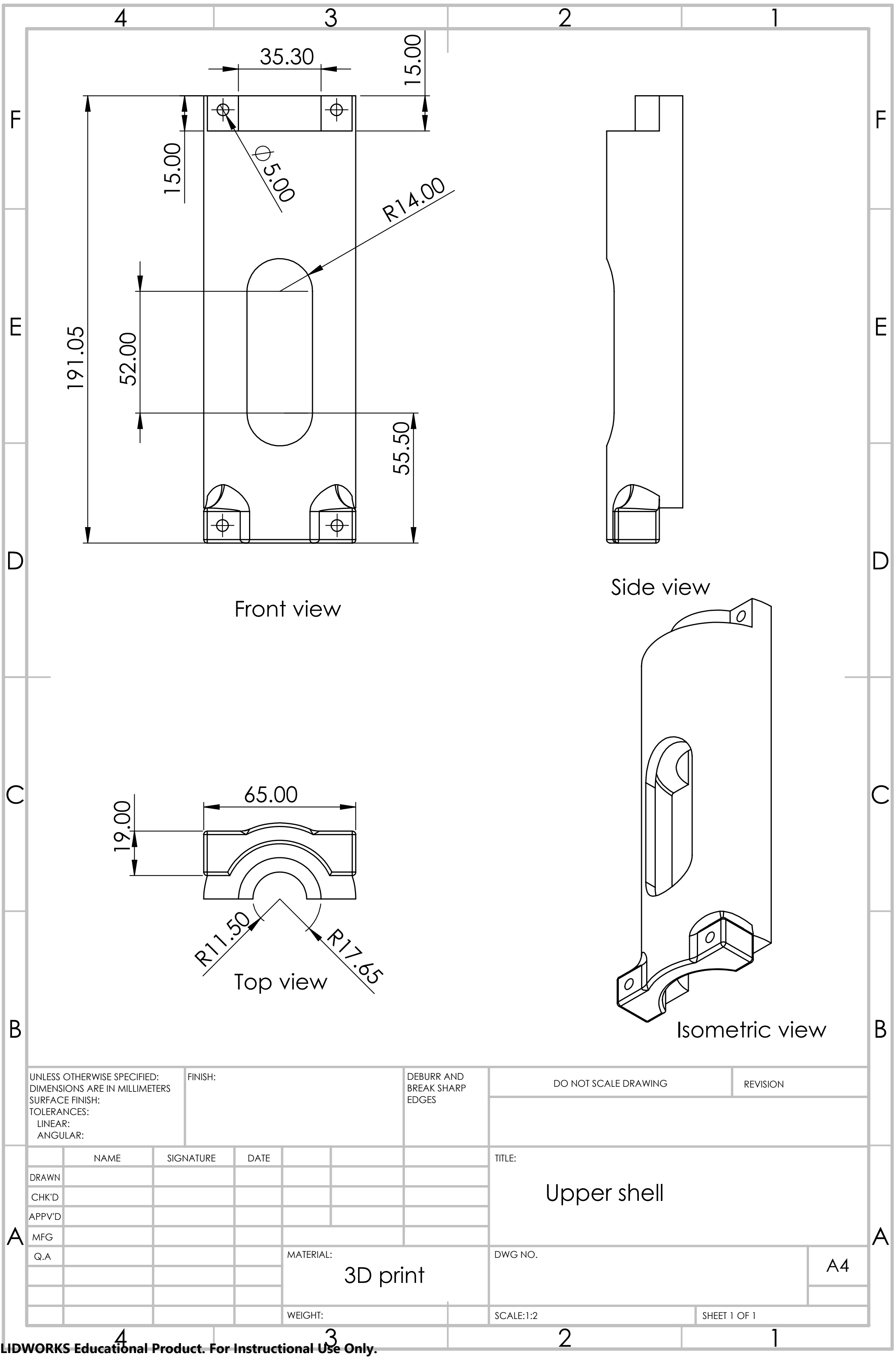

Figure 6.6: Engineering Drawing of Upper Shell

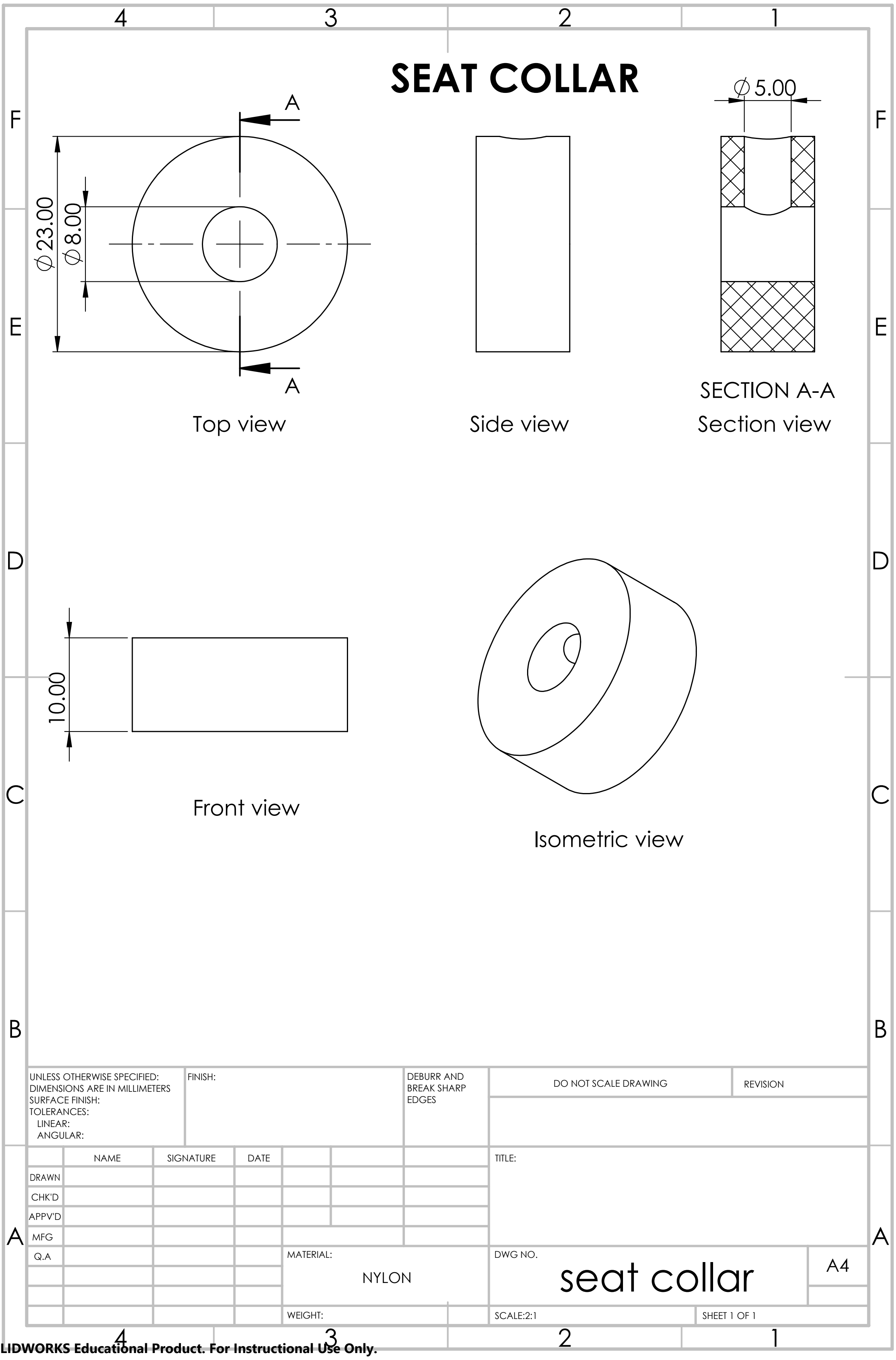

Figure 6.7: Engineering Drawing of Seat Collar

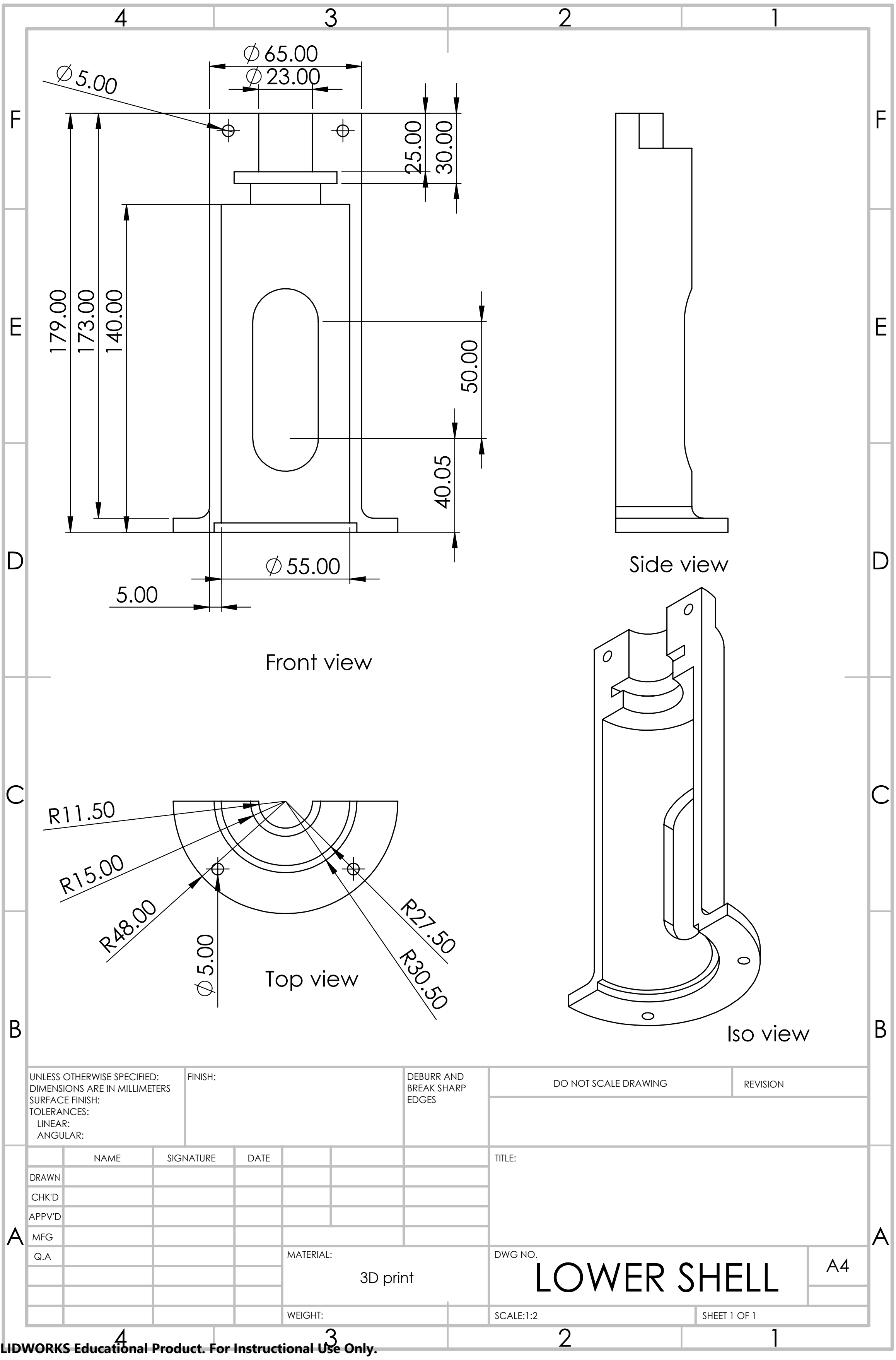

Figure 6.8: Engineering Drawing of Lower Shell

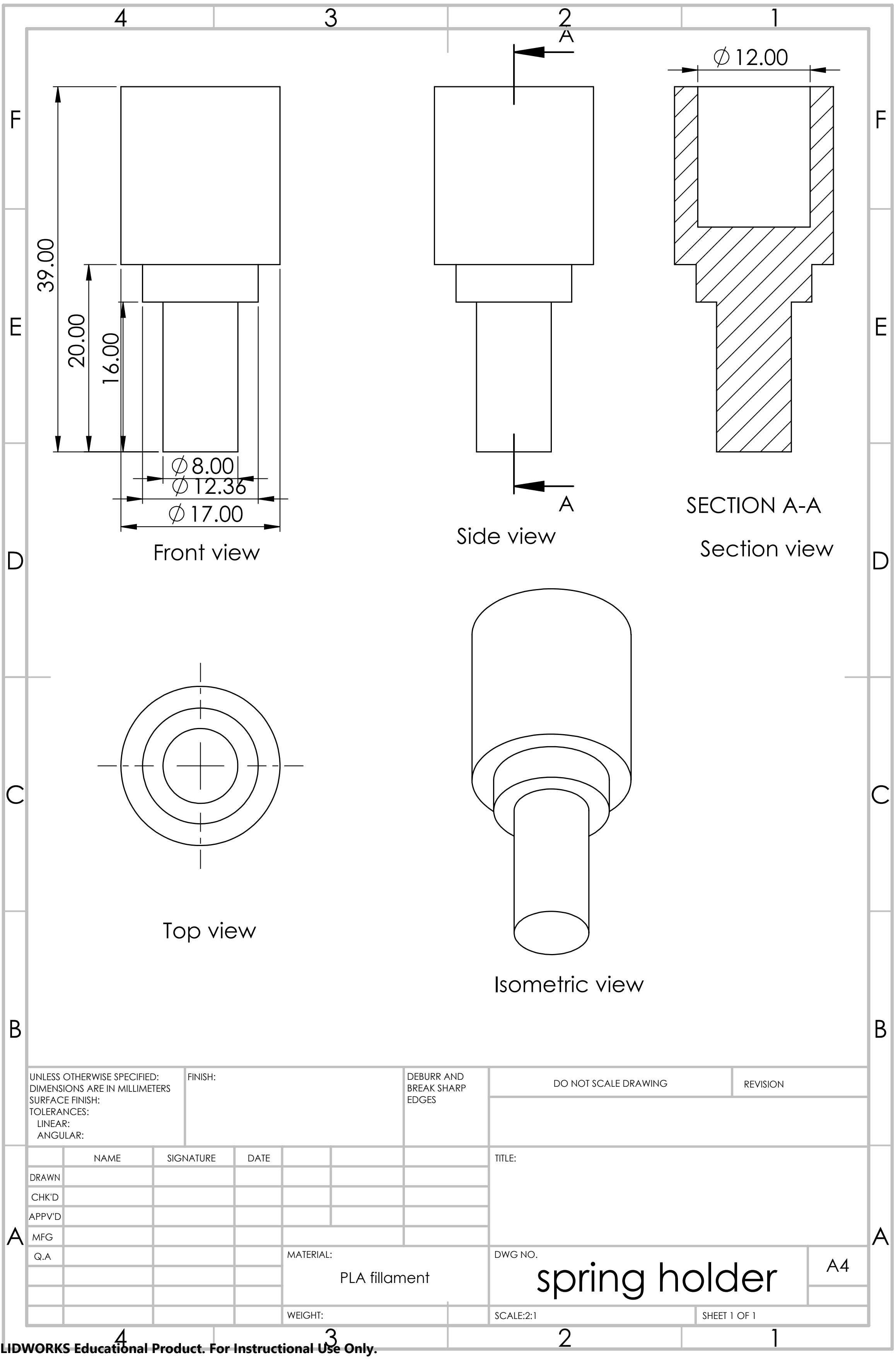

Figure 6.9: Engineering Drawing of Spring Holder

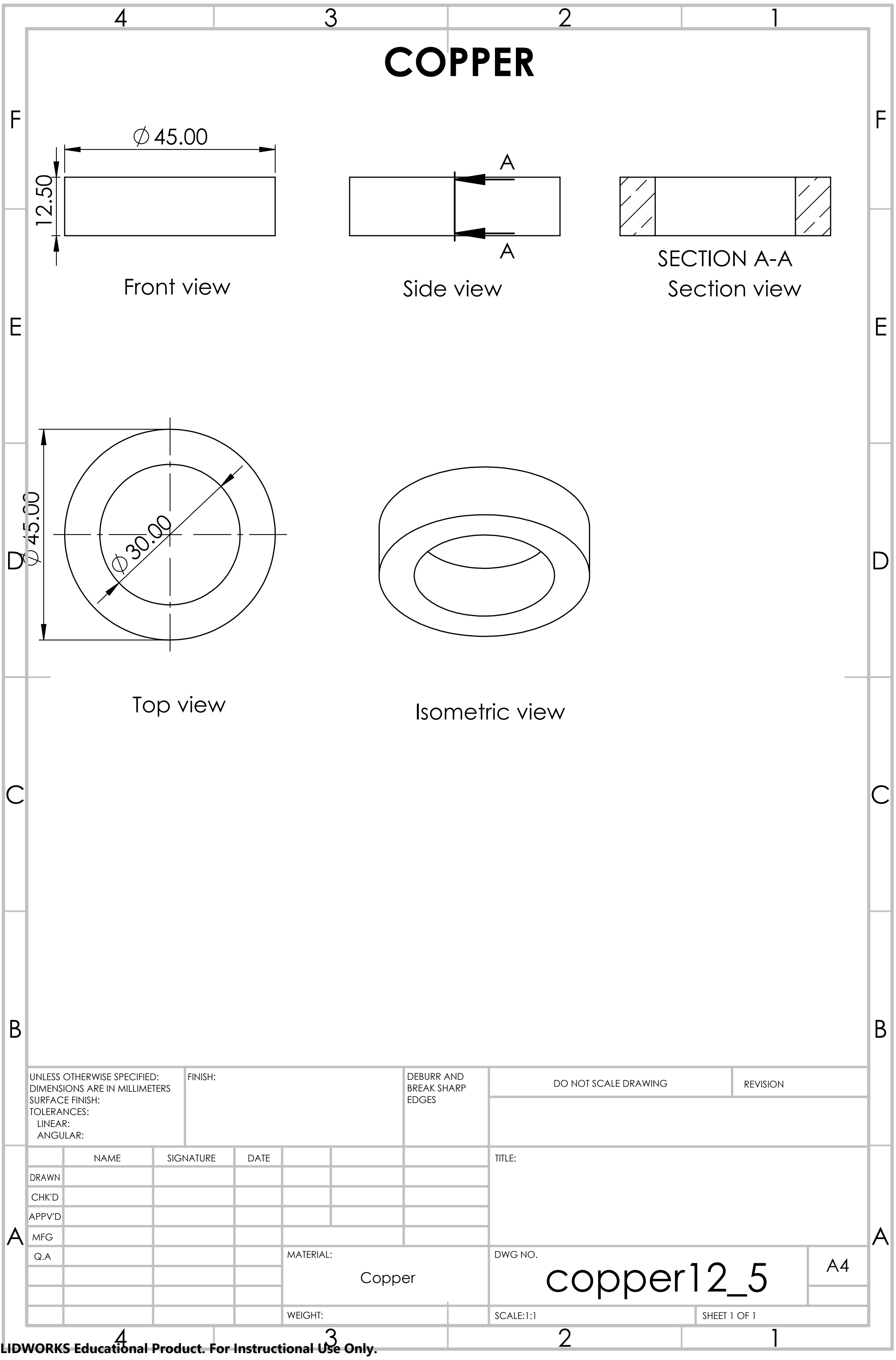

Figure 6.10: Engineering Drawing of Copper Component

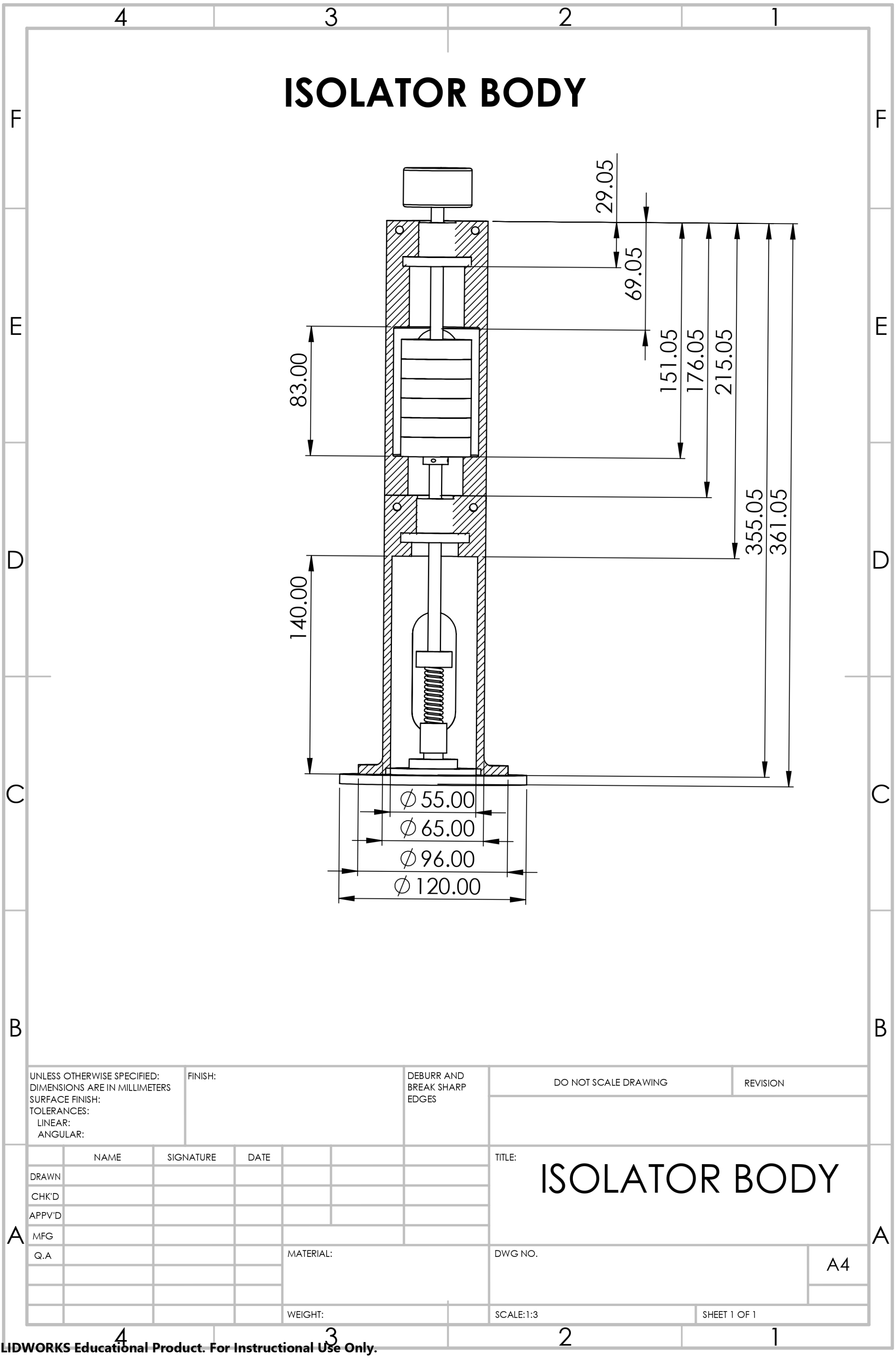

Figure 6.11: Engineering Drawing of Shake Table

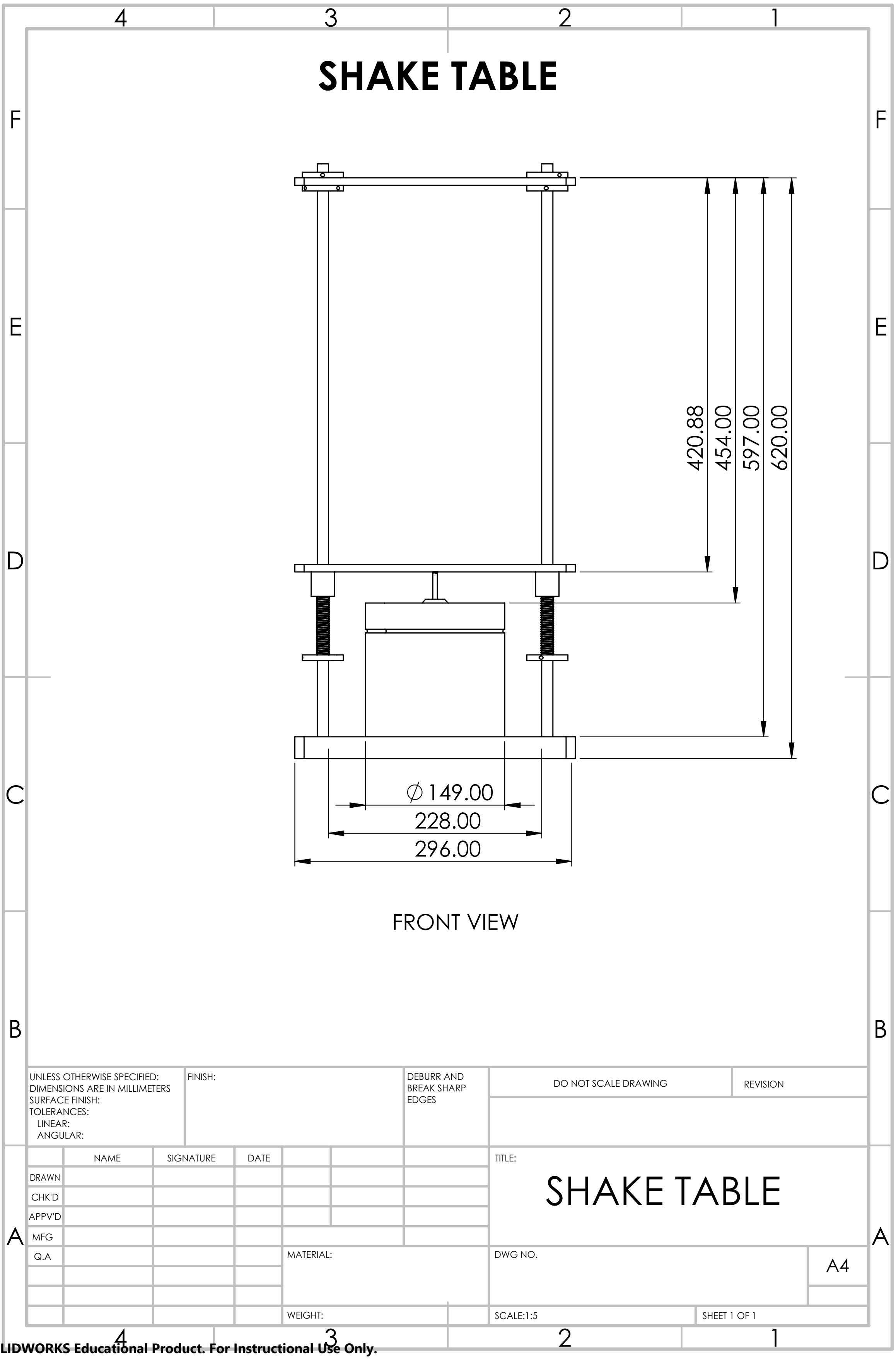

Figure 6.12: Engineering Drawing of Shake Table